Accepted Manuscript

Dust in the planetary system: Dust interactions in space plasmas of the solar system

Ingrid Mann, Nicole Meyer-Vernet, Andrzej Czechowski

PII: S0370-1573(13)00426-2
DOI: http://dx.doi.org/10.1016/j.physrep.2013.11.001
Reference: PLREP 1770

To appear in: *Physics Reports*

Accepted date: 13 November 2013

Please cite this article as: I. Mann, N. Meyer-Vernet, A. Czechowski, Dust in the planetary system: Dust interactions in space plasmas of the solar system, *Physics Reports* (2013), http://dx.doi.org/10.1016/j.physrep.2013.11.001

Dust in the Planetary System: Dust Interactions in Space Plasmas of the Solar System

Ingrid Mann[a,b], Nicole Meyer-Vernet[c], Andrzej Czechowski[d]

[a] *Department of Physics, Umeå University, Umeå, Sweden*
[b] *EISCAT Scientific Association, Kiruna, Sweden*
[c] *LESIA - Observatoire de Paris, CNRS, UPMC, Université Paris Diderot, Meudon, France*
[d] *Space Research Center, Polish Academy of Sciences, Warsaw, Poland*

Abstract

Cosmic dust particles are small solid objects observed in the solar planetary system and in many astronomical objects like the surrounding of stars, the interstellar and even the intergalactic medium. In the solar system the dust is best observed and most often found within the region of the orbits of terrestrial planets where the dust interactions and dynamics are observed directly from spacecraft. Dust is observed in space near Earth and also enters the atmosphere of the Earth where it takes part in physical and chemical processes. Hence space offers a laboratory to study dust plasma interactions and dust dynamics. A recent example is the observation of nanodust of sizes smaller than 10 nm. We outline the theoretical considerations on which our knowledge of dust electric charges in space plasmas are founded. We discuss the dynamics of the dust particles and show how the small charged particles are accelerated by the solar wind that carries a magnetic field. Finally, as examples for the space observation of cosmic dust interactions, we describe the first detection of fast nanodust in the solar wind near Earth orbit and the first bi-static observations of PMSE, the radar echoes that are observed in the Earth ionosphere in the presence of charged dust.

Keywords: cosmic dust, nanodust, solar system, dusty plasma, space measurements, space plasma

1. Introduction

The vast majority of elements heavier than oxygen in the interplanetary and interstellar space is contained in cosmic dust particles. Some cosmic dust particles initially form by condensation of the heavy elements from the gas, as occurs during late stages of stellar evolution e.g. in the envelopes of red giants, or in supernovae. The dust is expelled into the interstellar medium where particles are destroyed by sublimation, collisional fragmentation, sputtering and particles are formed by agglomeration, condensation, accretion and fragmentation of the larger dust. The processes depend on the properties of the surrounding medium, and for instance in dense and cool molecular clouds mantles of carbon bearing species can form onto smaller dust. The dust particles also offer a surface for chemical reactions taking place. In view of the number of complex phenomena the dust in the solar system only provides one very specific sample, but one that we have

(almost) at hand and that can be studied from spacecraft and sounding rockets in the interplanetary medium and space near Earth.

Dust particles in the solar system typically form by fragmentation of larger solid bodies: the comets and asteroids. A smaller amount of dust in the interplanetary medium enters the solar system from the surrounding interstellar medium. Dust particles of various origins are also present locally in the vicinity of comets and they are present in the ring systems, magnetospheres and atmospheres of the planets. The dust particles reside in the solar wind that fills the interplanetary medium, they enter the solar corona, the Earth's atmosphere and the atmospheres of the other planets. They are exposed to and interact with the local plasma environment in some cases revealing dusty plasma phenomena.

Among the dust particles, those with the smallest sizes are of particular interest because they have a large surface area compared to their mass, they provide a large surface for interactions, in many cases their physical interactions are influenced by small particle effects and they produce specific observational features. The smallest size of dust particles is not clearly derived from observations and it is not clear whether there is a gap to the molecular regime that is observed in some astrophysical environments (though not in the interplanetary medium). Nanodust of sizes smaller than about 10 nm consisting of order 10 000 atoms and less was only recently detected with in-situ space instruments and the lower size limit is not observed yet.

The studies of dust in our planetary system cover a wide range of disciplines ranging from cosmo-chemistry to observational spectroscopy and the field of research hugely expanded during the space era. This article will concentrate on discussing some of the physical processes that are particularly relevant to space observations. The article starts by addressing the questions of what dust particles are made of and of how they are measured and by summarizing their basic physical properties (Section 2). This is followed (Section 3) by a description of the region between the planets where the dust particles are found, the solar wind that they are embedded in and the asteroids and comets as their major sources. The subsequent sections investigate in detail the physical processes of dust charging in space (Section 4) and dynamics under the action of the corresponding electromagnetic forces (Section 5). The last section presents recent research stimulated by space discoveries: the discovery of nanodust in the solar wind and the dust - plasma interactions in the Earth atmosphere (Section 6). Unless otherwise stated S.I. units are used.

2. Dust definitions, observations and properties

2.1. What are dust particles?

Compared to what is called "dust" in the everyday life, the cosmic dust spans a wider size range. The size distribution of the solid objects in the solar system smoothly continues from the size of planetesimals to several nanometers. Many astronomers denote all solid objects, which are not spatially resolved in the observations as dust. To avoid confusion with other particles, for instance in a plasma, researchers often use the term grain for a dust particle.

The dust particles in the solar system are observed in a number of different ways leading to a complex terminology of dust and dust-related phenomena. This terminology

partly results from the different methods of traditional dust studies, like the meteor and the Zodiacal light observations and now is extended to include laboratory studies and space measurements (cf. Section 2.2). The complexity and absence of apparent logic of this terminology stems from the fact that it developed over time. The most commonly used terms related to dust are given below, whenever possible recent references are given. The given masses are converted to sizes (and vice versa) assuming that the dust particles are compact spherical particles with bulk density 2500 kg m^{-3}. This is a good estimate for the (abundant) silicate particles and is used throughout the text, if not stated otherwise.

- **Meteors** are, in particular, the light phenomena which result from the entry of solid particles from space into the atmosphere of the Earth. In a more general sense the expression describes all the observed phenomena associated with such an event, for instance radiometeors generated by backscattering of radio waves. The term meteor may also be used for these processes in other solar system objects. Bright meteors with luminosity equal to or exceeding that of the brightest planets (visual magnitude -4) are called fireballs or bolides [140]. The approximate mass ranges are [140] $> 10^{-1}$kg for fireballs, 10^{-8}kg $<$ m $< 10^{-1}$kg for optical meteors, and m $< 10^{-5}$kg for radio meteors (corresponding to radii, a $>$ 2 cm, 100 μm $<$ a $<$ 2 cm and a $<$ 0.1 cm).

- **Meteoroids** are solid objects that move in space between the planets (interplanetary space) and which size is considerably smaller than that of an asteroid and considerably larger than that of an atom or a molecule [140]. Masses are typically m $> 10^{-8}$ kg (radii, a $>$ 100 μm).

- **Meteoric Smoke** are dust particles of sizes presumably a few nanometers that re-condense from meteoric vapor in the Earth atmosphere [157].

- **Meteorites** are the solid remnants of meteoroids that reach the surface of the Earth without being completely vaporized; a micrometeorite is a very small meteorite or meteoritic particle with a diameter in general less than a millimeter [140]. The mass range of observed meteorites is 10^{-3}kg $<$ m $< 6 \times 10^{4}$kg [86] (radii 0.5 cm to 25 m).

- **IDP** (for interplanetary dust particle) is in a more specific sense often used to denote those cosmic dust particles that are collected in the atmosphere of the Earth. An example is shown in Figure (1). The collected IDPs have sizes 5 - 50μm [205]. In contrast to the larger micrometeorites, the IDPs show no obvious traces of melting from the entry process.

- **Zodiacal dust particles** are those particles in the interplanetary medium that generate the Zodiacal light brightness. The brightness is roughly proportional to the dust cross sectional area per unit volume in space and stems predominantly from the mass range 10^{-15} to 10^{-8} kg [55] (radii 0.5 μm $<$ a $<$ 100 μm).

- β **- meteoroids** are dust particles in the interplanetary medium that are strongly influenced by radiation pressure and as a result move in hyperbolic orbits, this is

typically the case for dust in the solar system in the 10^{-15} to 10^{-18} kg mass interval [140].

- **Nanodust** is often distinguished by its properties that are different from the larger dust. The term nanoparticle describes particles with 3 external dimensions in the size range 1 to 100 nm. A large fraction of the molecules or atoms in a nanoparticle are near the surface, so that the nanodust properties are determined by surface effects [106, 133].

- **Interstellar dust (ISD) particles** are those cosmic dust particles that are embedded in the interstellar medium, the space between the stars. They have nanometer to presumably centimeter size. Some interstellar dust particles can enter the solar system and are measured in the interplanetary medium [50, 117, 140, 141]. They cover the approximate size interval from 20 nm to 5 μm radius: the interstellar dust particles that are observed in-situ in the solar system have masses m $< 10^{-12}$kg. The interstellar dust with m $< 10^{-19}$kg is deflected from entering the solar system [142] .

This terminology reveals already the variety of different observation methods described in the following section.

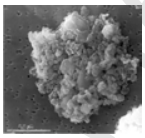

Figure 1: Scanning electron microscope image of a porous (fluffy) chondritic aggregate IDP ("interplanetary dust particle") collected in the lower stratosphere placed on a nucleopore-filter (background). Courtesy of the National Aeronautics and Space Administration, Particle W7029B13 (NASA number S-82-27575). Figure courtesy of Frans Rietmeijer, University of New Mexico, USA.

2.2. How are dust particles observed?

The dust measurements rely on a large number of different methods that cover different regions in space and different mass or size intervals of the dust (see Table 1).

2.2.1. Dust in the night sky

Cosmic dust is directly noticeable in the brightness of the night sky, at least in the absence of urban light pollution. Figure (2) shows the brightness of the night sky, as it appears when photographed with a camera equipped with a "fisheye" whole-sky lens. The unresolved brightness that appears in the night sky along the Zodiac, the Zodiacal light, results from scattering of sunlight off interplanetary dust particles. In the photograph it is seen as a band describing the largest dust density along the ecliptic, a reference plane within the solar system that us defined by the orbit of the Earth. The brightness along the band is brighter at the edges of the photograph which is caused by the dust observed at elongation 180 degree away from Sun; this effect is called the Gegenschein. The bright band oriented from the lower left to the upper right is the Milky Way, seen by its interstellar dust scattering and un-resolved star light. The tilt between the two

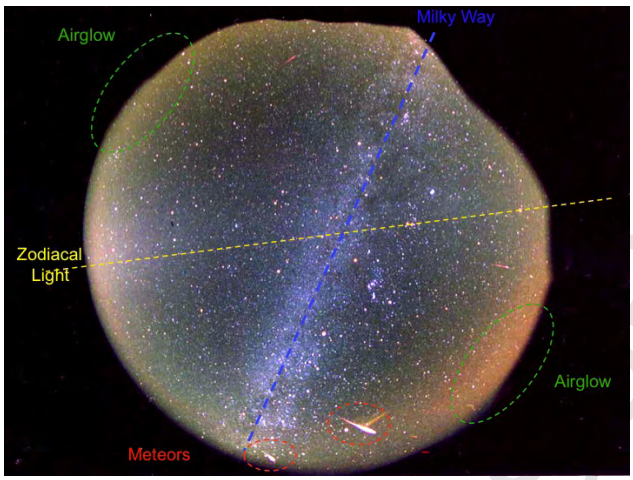

Figure 2: The night sky photographed from Mauna Kea, Hawaii with an analogue (35-mm film) camera with fisheye lens (focal length = 8 mm). The photograph displays the Zodiacal light, the Milky Way, four meteors and atmospheric OH emission (called airglow). Photograph courtesy of Masateru Ishiguro, Seoul National University, South Korea.

bands comes from the 60 degree inclination of the ecliptic plane relative to the galactic plane. The lower right and upper left parts of the image show atmospheric OH-airglow emission. Four meteors are seen near the bottom of the photograph. (For a compilation of the different light component of the night sky see [125].)

2.2.2. Astronomical observations of Zodiacal light and comets

Most of the Zodiacal light observed from near Earth originates from the dust in the approximate size range 1 to 100 μm located near ecliptic, at the distances from about 0.7 to 1.3 AU to the Sun [55, 126]. Some observations point closer to the Sun and show that the visible Zodiacal light continues smoothly into the solar corona [139]. The Zodiacal light is the most prominent unresolved extraterrestrial sky brightness from visible to far infrared. In the visible it is generated by the scattering of sunlight at the dust particles, in the near and mid infrared it is generated by their thermal emission. The observations at visible wavelengths provide information on the dust distribution and on the dust light scattering properties, like colour, albedo and polarisation [74, 230]. The brightness beyond wavelengths of several μm is generated by thermal emission. The thermal emission of dust particles follows approximately the spectral emission pattern of a black body described by Planck law. The thermal emission brightness of the dust located near 1 AU has its peak around 10 μm, the dust closer to the Sun at shorter and the dust at larger distance at longer wavelength, the observed brightness is the integrated line of sight from dust from the dust at different temperatures. Differently from the black body, the emissivity of dust particles is not a constant, but varies with wavelength, depending on the dust size and composition, so that the black body curve is superimposed with spectral features (discussed below in Section 2.3).

Figure (3) shows the observed sky brightness within spectral intervals around average 12, 24, 60 and 100 μm at 90 degree elongation for different latitudes from the ecliptic to

+/- 80 degree. Like the visible brightness (Figure 2) it describes the interstellar medium dust and the solar system dust brightness (Zodiacal light, sometimes also called Zodiacal emission). The Zodiacal light component peaks at 0 degree latitude, that is close to the ecliptic plane, a second peak at - 60 degree latitude is from the Milky Way brightness. Both components have different spectral variation, due to the hugely different temperatures. The Zodiacal light is highest at 24 μm, the Milky Way brightness at 100 μm. The shown fit to the Zodiacal light includes thermal emission from asteroidal, cometary and interstellar dust in the solar system [211].

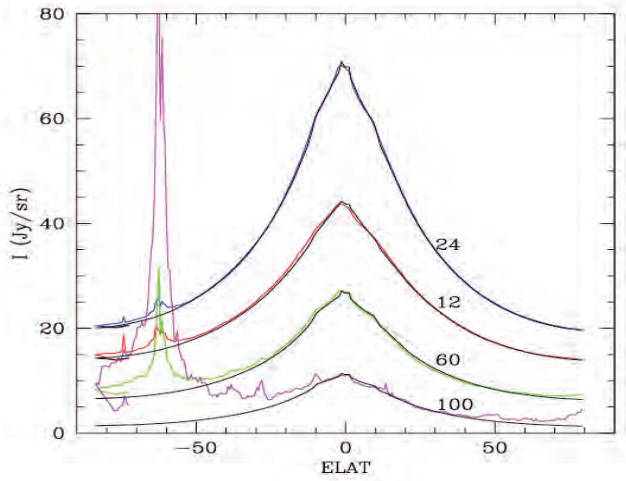

Figure 3: The infrared brightness measured with IRAS in comparison to a model of the Zodiacal light generated by thermal emission of dust in the solar system (solid lines). Measured brightness within spectral intervals around average 12, 24, 60 and 100 μm at 90 degree elongation in colour. The 0 degree latitude describes the line of sight lying within the ecliptic, the curves describe the brightness north and south to 80 degree latitude. Figure courtesy of Michael Rowan-Robinson, adapted from [211].

Most observations of the Zodiacal light beyond $\sim$ 10 μm are carried out beyond the atmosphere, from rockets [154] and from instruments on the satellites IRAS [12, 212, 213], COBE [78, 197, 104], IRTS [153] and ISO [197]. A compilation of all observations of the sky brightness until 1997 was prepared by Christoph Leinert and other members of Commission 21 *Light of the Night Sky* of the International Astronomical Union [125]. Since then, optical observations were carried out with improved camera systems [92, 93] and most recently the Planck satellite provided data of the Zodiacal light brightness from 30 GHz to 857 GHz [189] (i.e. wavelengths 1 cm to 350 μm). The 1997 review [125] also contains a discussion of the spatial distribution at the sky of the Zodiacal light and the structures observed in it. They are related to the spatial distribution of the dust which provides some clues on the acting forces and on the dust sources (discussed below).

The brightness of the solar system dust cloud that is observed from Earth in different directions at the night sky could also be observed from outside the solar system in the same way as astronomers detect the faint signals of dust disks around stars, some of which possibly harboring planets (Figure 4).

As discussed below, observations of the thermal emission are often used to compare the properties of dust in different regions, e.g. in the interplanetary space, near comets,

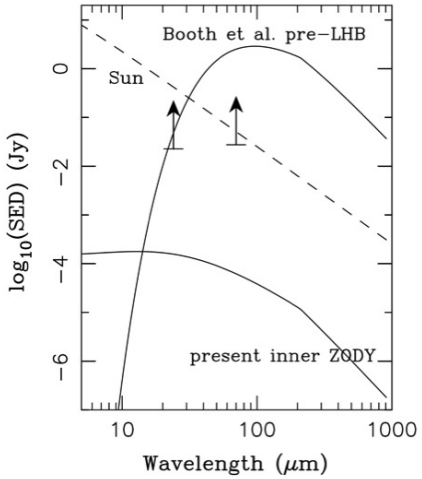

Figure 4: The spectral density distribution of the present inner solar system dust cloud (*inner zody*) and of an early solar system dust cloud model (*pre LHB* [18]) as seen by an observer at distance 10 pc from the Sun. The brightness of the present solar system dust cloud would be occulted by the Sun light shown as dashed line. The two arrows denote Spitzer telescope limits for detecting such a circumstellar dust brightness. Figure from [179], reproduced by permission of the AAS.

around other stars and in the interstellar medium. Since they can be observed from the ground in the visible range and in the spectral range of low atmospheric absorption around 10 μm, bright comets are often used to study dust properties (see e.g. [108, 113, 237, 73]).

2.2.3. Astronomical observations of the interstellar medium

Space astronomy has has made infrared observations an important tool to study the interstellar dust composition (see e.g. cite [43]) as well as the reaction of interstellar molecules (see e.g. [226]) like polycyclic aromatic hydrocarbons (PAHs) that were actually discovered in space based on infrared observations [3]. Figure (5) shows a mean spectrum of diffuse interstellar medium emission characterized by the emission bands of organic molecules, the emission of dust particles with $\sim$ 20 K temperature in equilibrium of emission and absorption in the radiation field of the surrounding stars and finally very small dust particles whose radiation balance is not in equilibrium (cf. Section 2.2.4 below).

Before the era of infrared astronomy, the interstellar dust was best studied by the interstellar extinction: the attenuation of star light that passes through the interstellar medium. The observed spectra of stars appear fainter and redder than expected because of the scattering off and absorption by dust particles distributed in the interstellar medium between the star and the observer.

The absorption and scattering of light are most efficient for the dust with sizes of the order of the wavelength of the light and hence the broad wavelength range over which the extinction is observed suggests that interstellar dust covers a broad size interval (for detailed discussion and references see [43, 133]). The extinction varies for different lines of sight, but the overall shape of the curve describing its variation as a function of the wavelength is similar for different lines of sight in the interval 0.125 μm $< \lambda <$ 3.5 μm and has a broad maximum around 217.5 μm. Most researchers explain this so-called

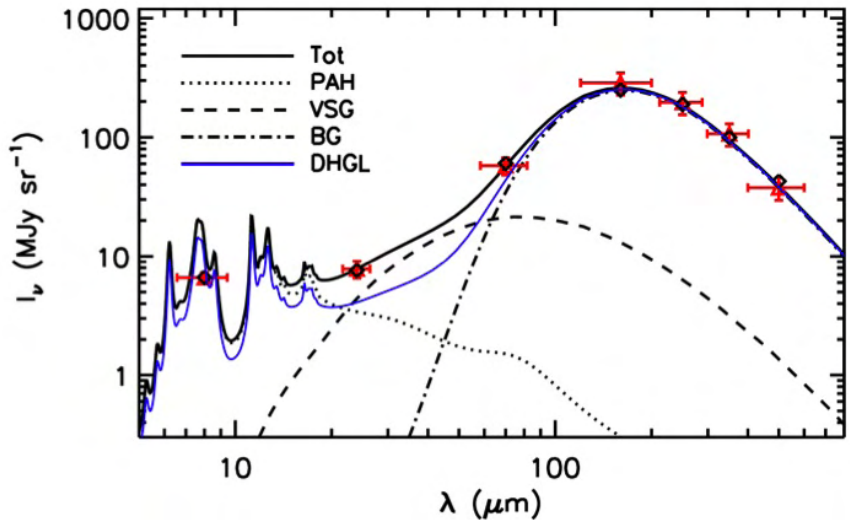

Figure 5: A mean spectrum of diffuse interstellar medium emission at the galactic plane obtained from Herschel observations and calculated emission from several dust components that contribute to a model. The observational data (red symbols) and the adjusted model brightness (black symbol) overlap. The model comprises three grain populations: polycyclic aromatic hydrocarbons (PAHs), small amorphous carbons representing the very small grains (VSGs), and big grains (BGs) that consist of amorphous carbons and silicates. The short wavelength emission results from PAH, the long wavelength emission from very small grains (VSG). Figure from [30], reproduced by permission of the AAS.

extinction hump as due to presence of dust grains with radii, a $< 0.1\mu$m. But in the laboratory it is also measured at larger cosmic dust samples, possibly produced by smaller nanometric inclusions that they contain [21]. Analyses of meteorite samples reveal that nanosized grains are embedded within the samples. Isotope measurements show that a large fraction of them predate the solar system (presolar grains [29], see Figure 6).

2.2.4. Nanodust

The interstellar extinction in the far UV is caused by nanodust with sizes $\sim$ 25 nm [133]. Evidence for the existence of even smaller nanodust in the diffuse interstellar medium comes foremost from its infrared emission whose flux in the near- and mid-IR ($\sim$ 2–60μm) can not be explained by the typically cool interstellar dust particles. The brightness stems from single photon emission from the nanodust that corresponds to temperatures much higher than equilibrium temperature. This so-called stochastic heating requires two conditions. The heat content of the grain should be smaller than the energy of surrounding photons, and the photon absorption rate should be smaller than the radiative cooling rate. In the interstellar medium, this is the case for dust with radii a < 5 nm [43, 130].

The "anomalous" galactic foreground microwave emission observed in the $\sim$10–100 GHz range may also possibly be caused by nanodust due to electric dipole emission when it

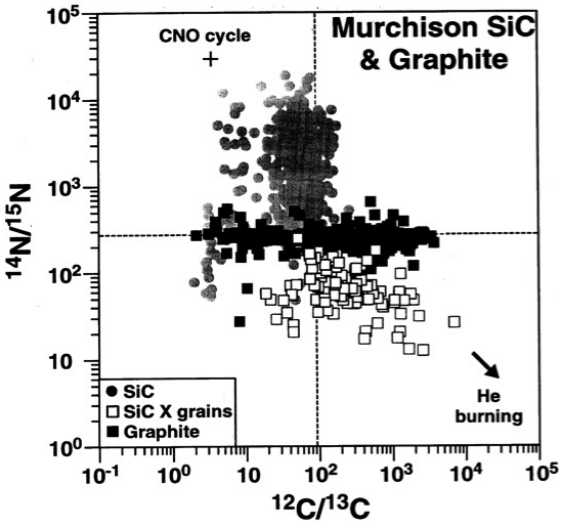

Figure 6: The Carbon- and N-isotopic compositions of SiC and graphite nanodust grains separated from Murchison meteorite samples. The deviation of isotope composition from those in the solar system shown with dashed lines points to the pre-solar origin of the grains. The cross and the arrow mark within the diagram indicate theoretical isotope ratios for the CNO cycle and He burning, respectively. The grain data are from Hoppe et al. (1994, 1995, 1996) and Nittler et al. 1995. Figure from [50], see references there, reproduced by permission of the AAS.

rotates [83, 133]. The impacts on the dust by the atoms of the surrounding gas at the temperature T make it spin at the angular frequency ω_d according to $I\omega_d^2 \simeq 3k_BT$ at thermal equilibrium, where the moment of inertia is $I = (2/5)ma^2$ for a spherical grain of mass m. As a result a non-symmetrical charge distribution on the grain produces radiation. A spinning grain with the electric moment p radiates the power $P = p^2\omega_d^4/12\pi\epsilon_0 c^3$, where c is the speed of light. The power steeply decreases with the increasing grain size since for spherical grains $I \propto a^5$. In interstellar environments only nanograins can rotate fast enough to emit at microwave frequencies.

It is also suggested that photoluminescence of nanodust produces a broad emission brightness in the $\sim$540–950μm range ("extended red emission, ERE"), but some of the nanodust materials that were proposed to generate the ERE are already ruled out on the basis of other rationals [234].

While this list of observed phenomena that are possibly explained with the existence of nanodust is not complete, in many cases the observation can also be explained in a different way, not including the presence of nanodust. Note that most of the reported detections of nanodust with astronomical observations are not a suitable method for detecting nanodust in the solar system [133].

2.2.5. Dust properties derived from interstellar medium gas

The bulk of the heavy elements in the interstellar medium are depleted from the gas and contained in the dust particles, this includes silicon, magnesium, iron and a large fraction of the carbon. In order to reduce the diversity of the models that describe the brightness observations of dust, it is helpful to estimate its element composition from the

observed composition of the gas. Absorption spectra of interstellar atomic and ionic lines observed along lines of sight long enough to contain a number of diffuse interstellar clouds provide information about the average element abundance in the interstellar medium gas component [201, 202, 238]. Assuming that the abundance of the elements in the interstellar medium is identical to the cosmic abundance, one can deduce that the missing heavy elements reside in the dust particles. Observationally derived gas-phase abundances are used in this way to estimate the dust composition (cf. [109, 132], see Figure 7).

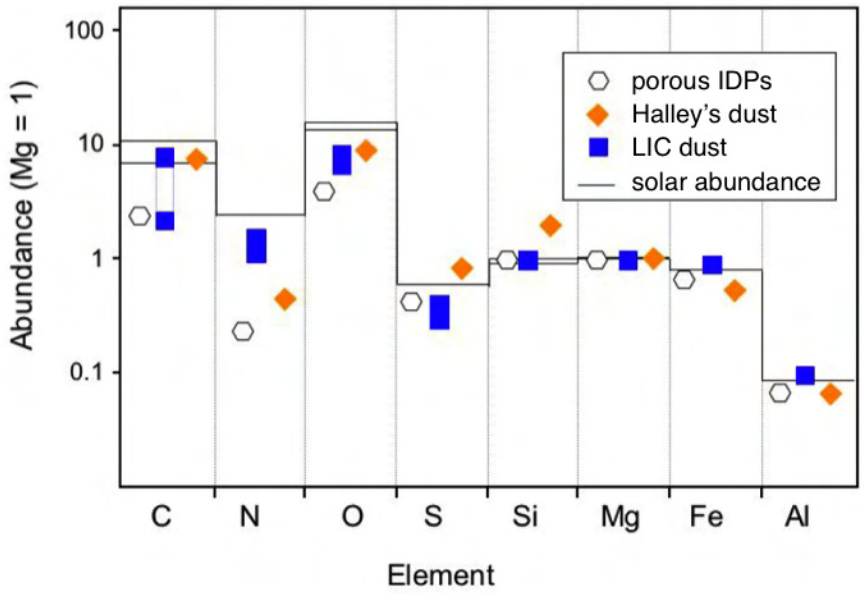

Figure 7: Element abundances of different types of cosmic dust derived by different methods in comparison to solar element abundance. Values are shown relative to Mg. The laboratory results shown correspond to measurements for a pristine class of collected IDPs (rhombes), from mass spectrometry instruments from spacecraft near comet Halley (diamond) and estimated for local interstellar cloud dust on the basis of observed abundances in the gas-phase (square), the last being model-dependent. Adapted from [109].

2.2.6. Dust and meteoroids entering Earth atmosphere

The dust particles crossing Earth orbit are studied for many years already on the basis of meteor observations [25]. The processes that occur when a meteoroid or dust particle enters the atmosphere depend on velocity, mass and composition of the entering object, but can be described as follows [25, 140]. In the tenuous upper atmosphere above about 400 km altitude the meteoroids are moderately heated by the impacts of individual atmospheric particles and some material is sputtered from its surface. In the denser lower atmosphere the meteoroid surface reaches evaporation temperature, meteoroid material and atmospheric particles collide, dissociate and ionize. This ablation stage occurs at about 140 to 60 km altitude and produces the typical meteor brightness. Parts of the meteoroid that survive until deceleration to less than 3 km/s continue a dark flight. The

remnant meteorite that hits the ground is altered on the surface. The collected meteorites are traced back to asteroids material of different stages of alteration [86].

Some remnants from the entry process remain within the atmosphere: small meteoroids and dust particles, gaseous species that originate from the meteoroids; and small meteoritic smoke particles that re-condense from the gas. Those dust particles (larger than the smoke particles) that are collected in the upper atmosphere show no significant alteration (the IDPs listed in Section 2.1). Since the ratio of surface, S to volume, V is $S/V \propto 1/a$ where a is the radius, small dust particles (typical sizes of order 10 μm) can efficiently re-radiate entry heat and reach only moderate temperatures during the entry process. Laboratory studies of meteorites and of collected interplanetary dust particles provide information on their origin, but also on the meteoric material that remains in the atmosphere [205].

Table 1: The mass range of dust and meteor observations in interplanetary medium and ionosphere.

Observation	Means of Detection	Dust Mass / Size
Spacecraft observation		
Dust detectors	impact generated charges	10^{-19}–10^{-11} kg
Plasma wave instruments	impact generated charges	$< 10^{-20}$–10^{-12} kg
Dust analyser	ion mass spectrum	$\sim 10^{-14}$–10^{-12} kg
Ballistic rocket observation		
UV photometers	scattered sunlight	size > 40 nm
Dust detectors	dust surface charges	10^{-24}–10^{-23} kg
Night sky observation		
Zodiacal light & Comets	scattering & thermal emission	size $0.5-100$ μm
Optical meteors	molecules, atoms & ions	10^{-8} kg – 10^{-1} kg
Fireballs	molecules, atoms & ions	10^{-1} kg – 10^{3} kg
Radar observation		
Head echoes	free electrons	10^{-9}–10^{-6} kg
Radar meteors	free electrons	10^{-12}–10^{-5} kg

2.2.7. In - situ observations from spacecraft

Dust in the interplanetary medium was observed in-situ from different spacecraft, most of them within the orbit of Jupiter and many of them near Earth.

A dust grain impacting at the speed exceeding a few kilometres per second a solid target such as a spacecraft, a larger grain, or an asteroid or planet, produces a shock compression wave which vaporises and ionises the dust as well as some material of the target

where an impact crater forms. This material then expands into the low-pressure ambient medium and charged components partially recombine [41]. In space measurements, the (residual) ionisation of the expanding cloudlet is used to detect the grain. This is applied in classical impact ionisation dust detectors (see [5] for a review) Other space instruments have also observed features that were attributed to dust impacts onto spacecraft, i.e. during comet and planetary rings encounters and in the interplanetary medium (see e.g. [70, 161, 180, 182, 183, 71, 223]). Motivated by observations, the physics underlying the dust observations with radio and plasma wave instruments has been discussed (see reviews [184, 164]), Observations have been recently refined by using a new generation of high speed radio receivers [243, 124]. The instruments typically detect impacts of particles of sizes of several nm and larger. The observations of nanodust will be discussed in Section 6.1.1 below.

The dust instrument onboard Ulysses which produced a large data set over more than a solar cycle (see [66, 64, 116] and references there) is described as an example for an impact ionization detector: For each impact it recorded a sequence of different charge signals measured within the instrument. Taking into account pre-flight laboratory measurements, the measured charge signals and their time sequence are used to estimate the dust mass and impact speed. Taking further into account the detector geometry and spacecraft velocity and orientation at the time of the impact provides an estimate of the dust velocities. In this way the mass was derived with a factor of 10 uncertainty and the velocity with factor of 2 uncertainty for dust of masses 10^{-19}– 10^{-11} kg. Even though the dust instruments utilize charge measurements, they only in few cases permit deriving information about the dust surface charge (see [5, 66, 116] and references there). The Ulysses instrument did not measure the velocity vector of the dust particles, but the detector geometry in combination with the information of the orientation of the spinning spacecraft at the time of the impact restricts the orbits of the dust particles that can reach the detector (Figure 8 on the left). This information was used to distinguish interstellar dust particles in the Ulysses measurements by means of their different trajectories from the solar system dust [64]. Ulysses offered a unique opportunity to identify the interstellar dust because the flux of the interstellar neutral gas was measured onboard the same spacecraft [235, 236] so that dust and gas flux directions can be compared (Figure 8 on the right).

Several dust instruments measure the time-of-flight mass spectra of the vapor that is generated by the impacts. While in principle the element composition of the dust can be inferred from the mass composition of the detected ions, this is complicated by the fact that the impact vapor contains both the dust and the spacecraft (target) material and that the impact ionization process is not well understood. The element composition of the cometary dust was firstly derived from space measurements based on mass spectra obtained during the space missions to comet Halley [224, 225] (see discussion below). More recent measurements with the Cassini Cosmic Dust Analyser (CDA) experiment primarily deal with dust particles in the vicinity of Saturn, for a review see [89]. Because with CDA the mass spectra are only measured for a fraction of particles impacting the instrument, very few mass spectra were observed in the interplanetary medium [82, 191].

Many of the instruments for observing the dust in the ionosphere of the Earth (see Section 6.2) also make use of charge measurements [81]. The instruments that are carried

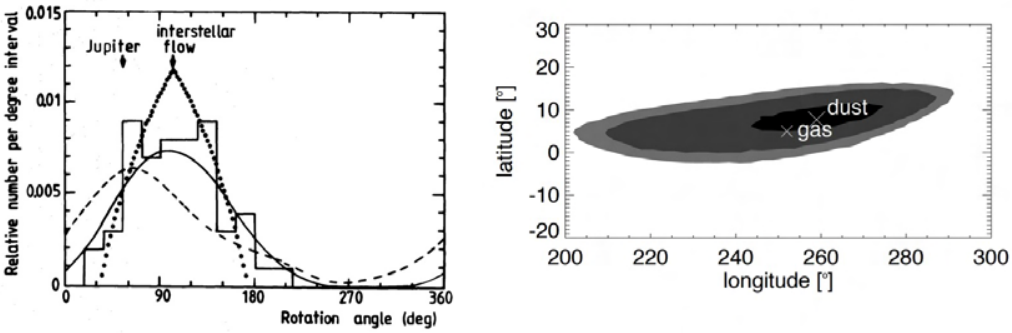

Figure 8: Interstellar dust measurements with the Ulysses dust instrument: the left figure shows the spacecraft rotation angle at time of impact for the particles identified as interstellar dust as histogram, the solid line shows a Gaussian fit to the data. The distribution of impacts from particles that would follow nominal interstellar wind direction is shown with the dotted line that peaks at 103 degree rotation angle. The dashed line, for comparison describes the Gaussian fit of the population of smaller dust grains measured that are associated to streams ejected from the vicinity of Jupiter, direction to Jupiter is also marked. The right figure shows the contour plot of impact direction of interstellar dust measured on Ulysses and Galileo with levels 1 sigma (black), 2 sigma (medium grey) and 3 sigma (light grey) in comparison to the interstellar upstream direction derived from Ulysses neutral gas observations, all in ecliptic coordinates. Figure on left from [64] reproduced with permission ©ESO; Figure on right from [50], reproduced by permission of the AAS.

on ballistic rockets observe much higher dust number densities of order 10^6 to 10^9 m^{-3} but with much smaller impact velocities. The instruments measure the current of the surface charge of impacting particles and do not separate single grain impacts. The dust flux is derived from the measured electric current by assuming a surface charge for the dust particles. The result therefore depends on the charge assumption. The impact velocities at rocket experiments are usually low, so that impact ionization is less efficient. It is quite possible, though, that secondary charges are produced even at this low impact speed and modify the current [79]. A further difficulty is that the very small grains are aerodynamically deflected from reaching the instruments [68].

2.3. What are the basic properties?

Studies of collected dust particles and of larger meteorite material suggest a guideline for estimating the dust composition. The interplanetary dust particles collected in the upper Earth's atmosphere commonly reveal an irregular, sometimes porous structure as well as heterogeneity in material composition on scales < 100 nm. Compounds frequently found in interplanetary dust are magnesium-rich silicates and silicon carbide, iron-nickel and iron-sulfur compounds, calcium- and aluminum oxides, and chemical compounds that contain a large mass fraction of carbon (e.g. carbonaceous species). Figure (1) shows an interplanetary dust particle that was collected in the upper Earth's atmosphere. This aggregate interplanetary dust particle consists of platy silicate grains embedded in a matrix of (partially fused) principal components and belongs to the class of so-called chondritic IDPs thought to originate from ice parent bodies with little internal material processing in comparison to, e.g. asteroids [206].

The abundances of many elements in meteorites are similar to those in the solar photosphere, and in the case of the most primitive class of meteorites, the CI chondrites, most elements abundances agree with the solar ones within a factor of 1.5, for many the agreement is even within a few percent [86]. Except for the volatile elements, the CI chondrites are taken as a chemical reference for bulk solar system matter element abundance [86], often also assumed cosmic abundance.

Since interstellar, cometary dust and primitive meteorites have similar element composition (Figure 7) and since they form in a similar way and have a common path of formation, their mineral compositions are often compared. Most cosmic dust particles contain a large fraction of silicates. Silicates are minerals that contain a silicon-bearing group (like SiO_2 or SiO_4) and that make up roughly 90 percent of the crust of the Earth. They are also a major compound of meteorites [86]). The stretching vibrations of $Si--O$ bonds in silicates produce spectral signatures (in this context often called features) near 10 μm in the emission, absorption and transmission spectra. Bending mode vibrations in the silicates produce feature between 16 and 35 μm. The silicate features are a tool to derive dust composition from astronomical observations, especially of comets [73]. While minerals are defined by both, the chemical composition and the form of its ordered atomic structure, the term amorphous silicate is often used in order to interpret astronomical observations. It denotes amorphous substances that have the same stoichiometric composition as the mineral. The amorphous silicates are often seen in the emission spectra. Crystalline and amorphous silicates in the dust form during different types of condensation or alteration processes [73, 75].

Figure (9) shows infrared spectra derived from astronomical observations compared to laboratory measurements of the samples of the Murchison meteorite [173]. Murchison is among the most chemically primitive meteorites that are rich in organic compounds. It is regarded to be a typical analogue of a class of asteroid material with reflectance spectra similar to 30 to 40 percent of observed asteroids [100]. The Murchison samples were shocked to different pressures so that some of the component minerals completely decomposed to an amorphous material. The measured infrared spectra vary depending on the shock pressure that was applied to the samples and it is suggested that similar alteration can occur during high velocity collisions in space or during entry of particles into the Earth atmosphere [221]. This comparison of comet and laboratory spectra suggests that the comets also contain silicates in different stages of processing [173]. Note that the astronomical data show only deviation from the smooth slope of brightness vs. wavelength. The Zodiacal light emission brightness provides fewer information on dust composition than the observations of comets. While observations in the vicinity of comets also include a large fraction of the small dust particles, the observations of the Zodiacal light brightness mainly cover larger particles, for which thermal emission is closer to that of a black body and hence the characteristic emission features disappear. Nonetheless small infrared features are also noticeable in the Zodiacal light and are explained with a mixture of different crystalline and amorphous silicates. The variation of the features with latitude and elongation of the observation suggests that the dust properties vary with the location within the interplanetary dust cloud [198].

The element composition measured for the cometary dust, has a larger abundance of the elements C, H, O, N than the meteorites. This suggests that the dust also contains a

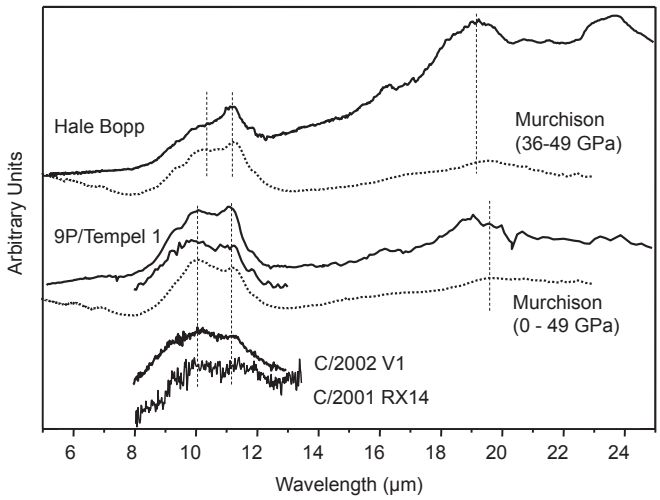

Figure 9: Comparison of comet observations (solid lines) and laboratory measurements of the Murchison meteorite samples (dotted lines). The upper laboratory spectrum is obtained from material shocked to 36 and 49 GPa, the lower is obtained from combining the measurements at samples shocked to different pressures up to 49 GPa. The observations are (top to bottom) comet Hale Bopp [136], comet 9P/Tempel 1 [136, 76], Comet C2002 V1 (NEAT) [85] and C 2001 RX_{14} (LINEAR) [85]. Vertical lines indicate the positions of the olivine spectral signatures (features). Figure adapted from [173].

significant fraction of carbon compounds. They possibly appear in the form of organics. In contrast to e.g. the interstellar medium observations, though (Figure 5) the Zodiacal light observations contain little information on the chemical appearance of the C, H, O, N.

3. Dust as a component of the planetary system

3.1. The solar wind and local interstellar medium

The solar environment is filled with the solar wind, which can be thought of as the outward extension of the solar atmosphere - a hot 10^6 °K corona, with pressure 10 orders of magnitude greater than that of the interstellar medium and thermal conductivity as high as that of brass. The physics of its expansion is far from being fully understood [152], [165]. The difficulty lies in the fact that the outer solar corona and the solar wind are weakly collisional plasmas. Outward from a few solar radii, the particle mean free paths are of the order of the heliocentric distance and as a result, the plasma is not in local equilibrium [152]. The transport of energy is not fully understood, so that a correct modelling must go beyond the usual (multi)fluid picture [187], [127] and requires elaborate kinetic treatments. The region around the Sun which is filled by the solar plasma and solar magnetic field is called the heliosphere, it extends $\sim$ 100 AU and larger (cf. Section 5.1). The solar wind is supersonic in the region the includes the orbits of the planets, i.e. inwards from the termination shock (cf. Section 3.2).

Solar wind measurements on space probes were made from inside Mercury's orbit to the outward frontier with the interstellar medium [204], [156] :The solar wind carries $\sim 10^9$ kg/s of protons and electrons, with a few percent of He^{++} ions and about 0.1 %

of heavier elements in various high ionisation states, with a nearly radial supersonic bulk velocity $V \sim 400$ km/s, and kinetic temperatures $T \sim 10^5$ °K at 1 AU. This amounts to a few protons per cubic centimetre at 1 AU, i.e. gas mass density $\sim 10^{-20}$ kg m^{-3}, roughly equal to that of dust.

The solar wind also carries a large-scale magnetic field $\mathbf{B}$, whose magnetic energy per unit volume $B^2/2\mu_0$ is of the same order of magnitude as the plasma thermal energy. The basic magnetic structure may be understood by viewing the Sun as a huge magnetic dipole (with higher-order magnetic components). Because of their high temperature, the solar corona and wind have a high electric conductivity $\sigma \simeq 6 \times 10^{-4} T^{3/2}$ Ωm^{-1}, yielding a very large magnetic Reynolds number $R_M = \mu_0 \sigma V L$ (at the spatial scale L). Namely, the time for the magnetic field to diffuse over a distance L, $\mu_0 \sigma L^2$, is much greater than the dynamic time L/V, so that the magnetic field is "frozen" in the medium: the plasma can move freely along the magnetic field lines, but any motion perpendicular to the field lines carries them with the plasma. The magnetic field lines tend to be dragged by the flow, yielding a radial magnetic field which varies with the distance r as $B_r \propto r^{-2}$ (since $\nabla \cdot \mathbf{B} = 0$). The solar rotation, of period approximately 25 days (angular speeed $\Omega \simeq 2.7 \times 10^{-6}$ rad s^{-1}) complicates this picture. Since at distance r and heliolatitude θ, the solar rotating frame has the azimuthal speed $v_\phi = \Omega r \cos\theta$, the dragging of magnetic field lines produces an azimuthal magnetic field $B_\phi = B_r v_\phi / v_r$, whence

$$B_\phi = -B_r \times \Omega r / V \tag{1}$$

This produces the basic 3-D magnetic structure, called Parker spiral [186]: the magnetic field lines follow Archimedean spirals wound up on the surface of cones of half-angle equal to the co-latitude. The radial magnetic field component, remarkably independent of the heliolatitude [8], varies with the distance r_{AU} (in astronomical units, i.e. $r_{AU} \simeq r/1.5 \times 10^{11}$) as

$$B_r = 3 \times 10^{-9} \times r_{AU}^{-2} \ \ \mathrm{T} \tag{2}$$

and B_ϕ follows from Eq.(1). The magnetic field is thus nearly radial much closer than the distance $r \sim \Omega/V$, and nearly azimuthal much farther out. Because of the basic solar magnetic dipole configuration, the sign of $\mathbf{B}$ is opposite in the two hemispheres, producing a discontinuity in magnetic field: a current sheet (satisfying $\nabla \times \mathbf{B} \simeq \mu_0 \mathbf{J}$). Close to the Sun, the current sheet follows the shape of the magnetic equator or the neutral line. Since the latter does not coincide with the solar (rotational) equator, so that different parts of it lie in the different hemispheres, the current sheet is drawn out by the solar wind into a wavy surface whose intersection with a meridian plane has a wavy shape - varying in time at the frequency Ω and in distance at the wavelength $2\pi V/\Omega$. Hence, further out the heliospheric current sheet resembles a spinning ballerina skirt.

The solar magnetic structure, which drives that of the solar wind, changes with the solar cycle. At the minimum of solar activity, the basic structure is dipolar with a magnetic dipole axis making a small angle α with the rotation axis, which is normal to the ecliptic plane (i.e. the ballerina skirt has a latitudinal extension α). During the solar cycle, the angle between both axes increases, multipolar components become more conspicuous, and large localized magnetic concentrations appear and move on the Sun, culminating at solar

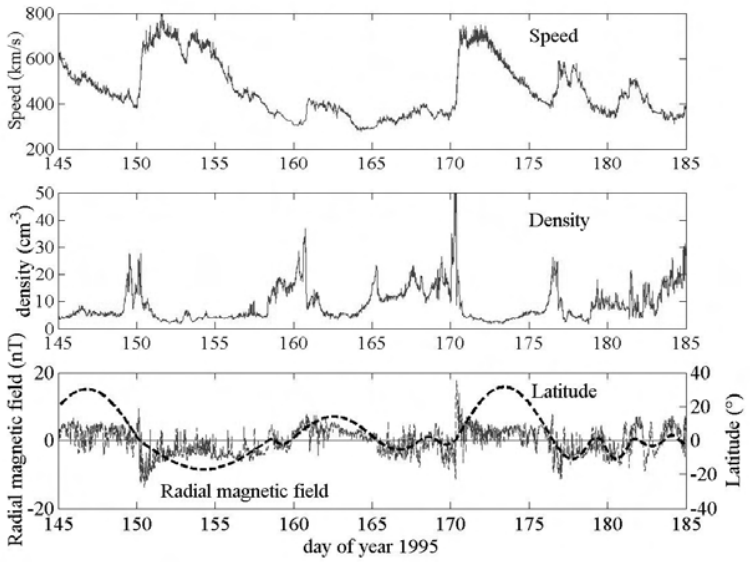

Figure 10: Proton velocity (top panel) and electron density (middle panel) measured on the spacecraft WIND in June 1995, at 1 AU from the Sun in the ecliptic. The bottom panel shows the radial component of the magnetic field and the opposite of the latitude of the heliospheric current sheet with respect to the spacecraft (which is close to the ecliptic). (Adapted from [165])

.

activity maximum when the dipolar structure begins to reverse [219]. Therefore the signs of B_r and B_ϕ in Eqs(1)-(2) reverse every 11 years, as does the solar magnetic dipole.

This basic structure is further complicated by various perturbations (Figure 10). Firstly, since the magnetic field of the basic dipolar structure is nearly radial in polar regions, the outgoing wind can flow unimpeded along the magnetic field lines, at a high speed. In contrast, in the equatorial regions, the outgoing wind encounters a nearly normal magnetic field, which - forced by the frozen magnetic field - must be drawn outward to open the magnetic field lines, resulting in a smaller speed. As a result, the solar wind flows in two basic states: "fast" ($V \simeq 800$ km s^{-1}), and "slow" ($V \simeq 400$ km s^{-1}) which, remarkably enough, carry similar wind energy [123]. The interaction between fast and slow winds further complicates the three-dimensional structure, since in the regions of interaction, like the corotating interaction regions, the compressions and depressions produce shocks [208]. This is illustrated in Figure (10), which plots one month of data from the spacecraft WIND, showing the two wind states with density peaks associated to compressions in the interaction regions. Accordingly the shape of the current sheet varies faster than with the simple periodicity described above (see [9]). The other kind of large scale perturbations is produced by coronal mass ejections, which produce huge magnetic clouds and associated shocks propagating in the heliosphere. Coronal mass ejections are more frequent at solar activity maximum [36]. To these large scale perturbations small-scale waves and turbulence are superimposed [24]. Note, that the dust temperatures in the solar system are not determined by the solar wind temperature, but by the balance of photon absorption and emission.

The space beyond the heliosphere − the interstellar medium − contains within 15 pc ($\simeq 3\times10^6$ AU) around the Sun at least 15 different clouds defined as parcels of interstellar gas with homogeneous kinematical and physical properties [203]. Two of the clouds that probably overlap are located in the immediate neighborhood of the Sun [120, 170]. The gas temperatures are rather warm ($\sim$ 7000K [200]) and the estimated dust densities are between $10^{-25} - 10^{-23}$ kg m^{-3} [50, 121, 109, 141, 122, 131]. The content of the interstellar medium in the vicinity of the Sun, that is also denoted as Local Cloud, streams toward the heliosphere (see Figure 11), whose structure and boundary with the interstellar medium is further described in Section 5.1.

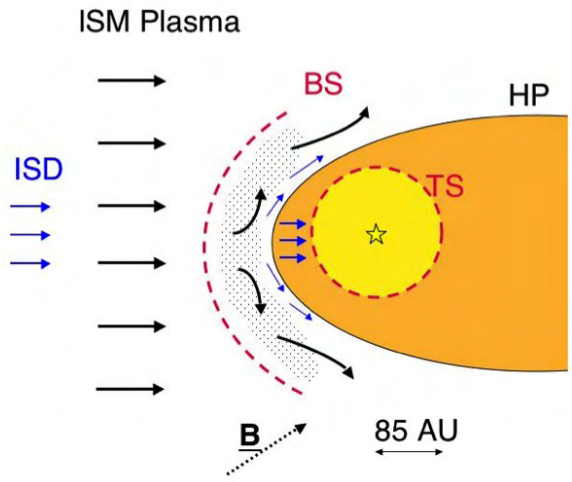

Figure 11: The region around the Sun that is filled with the solar wind is denoted as heliosphere.This sketch of the heliosphere in the surrounding thin, warm plasma of the interstellar medium is suggested by model predictions and shows the termination shock (TS), the heliopause (HP), and the interstellar medium (ISM) plasma bowshock (BS).

3.2. Planets and small solar system objects

The solar wind engulfs the planets and a host of smaller objects, the vast majority moving close to the ecliptic. An overview is sketched in Figure (12). The terrestrial planets Mercury, Venus, Earth and Mars are located at 0.39, 0.72, 1 and 1.5 AU from the Sun (where 1 AU is the average distance Sun - Earth). The outer giant (gaseous) planets Jupiter, Saturn, Uranus, and Neptune are at average distances 5.2, 9.5, 19 and 30 AU. They have numerous dust rings [20] and orbiting satellites (moons). A large number of small solar system objects orbit the Sun between the orbits of Mars and Jupiter: the asteroid asteroid belt. Objects in the outer solar system beyond the orbits of the planets (trans-Neptunian objects) are mainly attributed to the Kuiper belt and the Oort cloud as described below in this section.

The gaseous planetary environments are ionized by the solar radiation, producing ionospheres. The ionospheres are mostly shielded from the direct impact of the solar wind, since most planets have a significant global magnetic field, with a large dipolar component. The corresponding Lorentz force deviates the incoming solar wind particles,

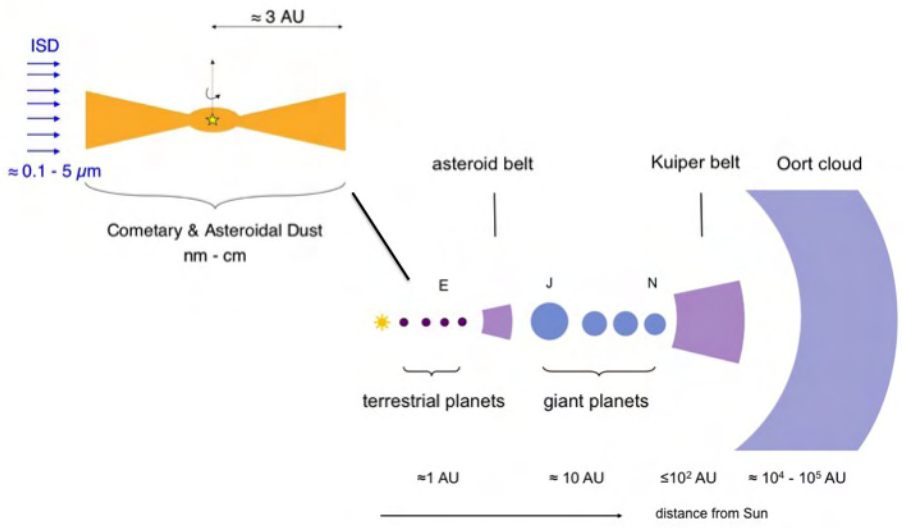

Figure 12: Sketch of the planetary system with the ecliptic plane of planetary orbits viewed edge on. The majority of interplanetary dust is located within the orbits of the terrestrial planets and the dust cloud is rotationally symmetric to an axis through the Sun perpendicular to the ecliptic. It number density is highest near the ecliptic. Adapted from [141].

making the solar wind slow down and stop ahead of the planet, and be deflected on the flanks. Because of the plasma and magnetic field being frozen together, this produces a region around the planet, the magnetosphere, made of plasma magnetized by the planet's own magnetic field where the solar wind does not penetrate (or weakly so). At the frontier of the magnetosphere - the magnetopause, the magnetic pressure holds the incoming solar wind plasma in front of the planet, producing a shock ahead. The magnetopause distance r_M can be estimated by equating the effective dynamic pressure of the solar wind (of mass density ρ, velocity V), ρV^2, to the effective magnetic pressure $(2B)^2/2\mu_0$, of the planet's magnetic field at the magnetopause distance r_M, with $B = (\mu_0/4\pi)\mu/r_M^3$ (the effective magnetic field is doubled because of the current sheet carried by the magnetopause) [165]. This estimate yields magnetopause distances close to the observed values. The extension of the Earth magnetosphere is of order 10 Earth radii at the sub-solar magnetopause stagnation point. In the case of the Earth, most of the dust particles can probably pass the magnetopause, and so do the larger meteoroids. The presence of the ionosphere (and of the atmosphere), on the other influences the escape processes of particles from the planet. A planet is a more direct dust source when it has both a solid surface and no significant atmosphere to protect it from interplanetary dust impacts. This is the case of Mercury, because of its low surface gravity and high temperature due to its close proximity to the Sun.

The Moon may serve as an example for the dust production from the surface of a small solar system object. Contrary to many other planetary satellites, the Moon does not lie

in the protecting environment of its planet (i.e. the magnetosphere, described below). In a similar way as for the asteroids and other small solar system objects, solar wind particles and interplanetary dust directly impact onto its surface. Dust particles impact the Moon's surface at typical relative speeds on the order of 30 km/s (the Earth's orbital speed), so that a grain impact produces a crater exceeding the mass of the impacting grain by 3 orders of magnitude. Dust particles ejected at speeds exceeding the escape speed ($(2MG/R)^{1/2} \simeq 2$ km/s) form a dust cloud around the Moon; the particles with smaller speed return to the surface [67]. The number and size distribution of micro-craters measured on lunar surface samples provide a record of the dust impacts over long time and are considered when estimating the dust flux near 1 AU (see [62] and references given there).

For most planetesimals, with diameter smaller roughly 300 km, the gravity forces are not strong enough to ensure a spherical shape. Their gravity is not either sufficient to retain an atmosphere, so that they are not protected from the impacts of solar wind particles and solid bodies. The low surface gravity enables the ejected debris to escape. The impacts of dust particles then lead to ejecta production. The small solar system objects also generate dust by mutual collisions. The asteroids in particular also are fragmented by mutual collisions and produce fragments over a large size interval.

The trans-Neptunian objects, based on their properties, are classified in different categories [174]. Most of them are potential predecessor of comets, having a large content of ice they become active when their orbits cross the inner solar system. For the sake of this discussion here, it is sufficient to mention that dynamically one distinguishes the Kuiper belt of objects in orbits within roughly 30 degree inclination from the ecliptic and within 50 AU from the Sun and the Oort cloud of objects further out. Similar to the asteroid belt, also collision of Kuiper belt objects and their impact ejecta generate dust fragments. The latter process gains importance in comparison to the collisions, because the velocities of the mutual collisions of objects in bound orbit are small compared to those in the inner solar system [241]. The Oort cloud is postulated in order to explain the observations of long-period comets, the Kuiper belt is seen as a source of short-period comets.

Comets are generated by planetesimals that are conglomerates of dust and ices, that pass sufficiently close to the Sun to sublimate their surface layers, liberating molecules and dust. Molecules blow away - unimpeded by the small gravity of the object, producing a huge expanding atmosphere in which complex chemistry acts in the presence of solar ionising radiation. Ionisation produces an ionosphere - of size much larger than the nucleus itself, whose electric conductivity excludes the solar wind magnetic field, making the wind stop ahead of the comet and sweep around it. So do the magnetic field lines frozen in the wind, which bend round and produce a long tail antiparallel to the solar direction, that guides the cometary ions. Ludwig Biermann's observation that comet tails always point straight away from the Sun (with a small aberration angle), behaving as distant solar wind probes, played a major role in early studies of the solar wind [16]. Note also that the solar wind is affected by the comet far ahead, because it picks-up cometary ions via its magnetic field, and the corresponding mass loading slows it down.

The expanding gas drags out dusty material, some of it subsequently fragments [222]. The micrometer dust grains, which contribute the most to the visible dust tail, are mainly driven by the solar gravity and radiation pressure, the latter reducing the effective grav-

itational attraction (cf. Section 5.2). The motion of ions along the solar magnetic field and the dust trajectories shaped by gravity and radiation pressure force produce the respectively straight and curved plasma and dust tails (shown in Figure 13), whose size can exceed the size of the nucleus by more than 6 orders of magnitude. Since the nucleus itself follows a trajectory determined by solar gravity, dust grains follow orbits that are more open than that of the nucleus. The large width of the dust tail is due to the fact that the solar radiation pressure is different for grains of different size and composition, and that grains emitted at different times follow different trajectories.

The sizes of comet bodies are typically on the order of a few kilometres across, a notable exception are the sun–grazing comets, observed in large number by the coronagraph telescope on board SOHO the vast majority when falling into the Sun [17, 112]. They are produced by solid objects of sizes several metres and because of the proximity to the Sun reveal an interesting example of the interactions of cometary dust with the solar wind Note that the transition between comets and asteroids is not so clear as it might seem [98], [99].

Figure 13: Comet Hale-Bopp 6 April 1997. The blue part of the tail is from ions carried with the solar wind. The white, bended tail is from dust particles deflected by gravity and radiation pressure force. Figure courtesy of Nicolas Biver, Observatoire de Paris, Meudon, France.

3.3. The major solar system dust components

Meteor observations and in-situ measurements from spacecraft show that the dust flux near Earth orbit covers a large mass range and this is explained by the size distribution of collision fragments of the small solar system objects (see e.g. [62, 25, 94]).

Interplanetary dust particles initially move in orbits similar to that of the parent body from which they form. Considerations of the dust dynamics in Section 5 will reveal that a large fraction of the dust of sub-μm sizes with masses below $\sim 10^{-16}$ kg is ejected from the solar system within a short time either by the radiation pressure or by electromagnetic forces. Most dust particles that are not strongly influenced by the Lorentz force experience only moderate changes of the orbital plane and stay in low inclination orbits relative to the ecliptic. As a result the interplanetary dust cloud that is observed in the Zodiacal light is concentrated toward the ecliptic plane of the solar system. The influence of the radiation

pressure increases the eccentricity of the orbit. Gravitational perturbations change the orbital elements (primarily the argument of the perihelion and the longitude of ascending node). A uniform distribution of these two orbital elements results in a number density distribution that is rotational symmetric relative to an axis through the Sun. For the very large grains, meteoroids, the outward radiation pressure (proportional to surface) becomes negligible with respect to the gravitational attraction (proportional to volume), so that they follow orbits rather close to that of the parent comet [25]. Their trails remain for long time, especially those related to the comets in periodic orbits (see e.g. [199]). The yield meteor storms when they intersect the Earth orbit. The asteroid fragments also follow similar orbits as their parent objects.

The larger dust particles stay within the solar system for long time, though they survive on time spans small compared to the age of the solar system. The processes that limit the lifetime of the dust particles that are in bound orbit about the Sun are: (i) fragmentation during mutual collisions, (ii) migration toward the Sun within 10 000s years and longer as a result of the Poynting-Robertson force (cf. Section 5.2), and (iii) destruction by sublimation and sputtering by energetic particles. The lifetime of dust particles with masses $> 10^{-8}$ kg is limited by collisions [62]. The Poynting Robertson effect limits the lifetime of the smaller dust particles ($< 10^{-8}$ kg). Observations near Earth orbit and from Earth are described in models of a flux versus mass curve at 1 AU which can be explained by these processes [62, 25, 94]. Water ice and other volatile elements in cometary dust typically sublimate within short time after ejection from the comet. The vast majority of refractory dust constituents sublimate at roughly < 0.2 AU and the distance where the particles fully sublimate, typically at a few solar radii from the Sun, depends on the dust size, composition, and structure [147, 150]. The majority of comets and asteroids is located outside from Earth orbit and so it would be natural to assume that the dust particles are produced there. But model calculations show that the dust measured in the inner solar system cannot origin solely from the dust coming inward from the outer solar system (due to the Poynting-Robertson effect) and its collisional products. Comets and their meteoroids most likely provide the local source inside 1 AU [94].

The distribution of the parent objects is one of the reasons for small spatial structures in the overall Zodiacal brightness distribution. The structures are caused by a large number of dust particles still having the orbital distribution of the parent body as illustrated in Figure (14). The structures were firstly noticed in the observation of the IRAS satellite as small enhancements in the slope of the thermal emission brightness as function of ecliptic latitude and denoted as IRAS dust bands (or asteroidal dust bands). They were regarded as a proof for the contribution of asteroidal dust to the Zodiacal light (see discussion below). Another process to cause local structures in the Zodiacal light brightness is that the dust particles are trapped in resonance with a planet (similar to the resonance that causes the Trojan asteroids). The brightness enhancements are small and only recently discovered with refined infrared observations [125, 199, 189].

Within the region of planet orbits explored from spacecraft, the interstellar dust particles are the major dust component beyond roughly 3 AU. Most likely they are also the major dust component beyond the region of observations. The motion of the Sun relative to the surrounding interstellar medium causes a flux of neutral gas and dust into the plan-

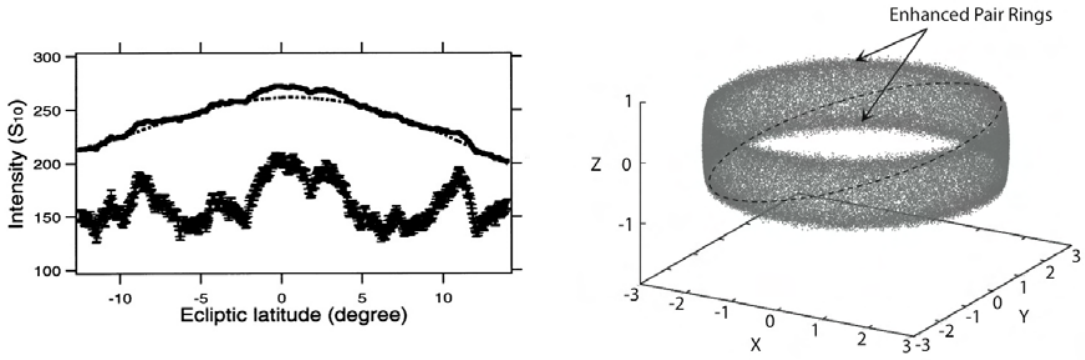

Figure 14: First observation of asteroid bands in the visible Zodiacal light ([93]. The intensity as function of ecliptic latitude is shown on the left. The upper curve shows the observed brightness profile and the smoothed background (dashed curve), the lower curve shows the difference between observed and smoothed brightness, error bars in the lower curev are scaled by a factor of 5 and shifted 150 counts. The sketch on the right shows how dust debris particles from one asteroid family form a torus structure, because their orbits have similar inclination, eccentricity and semi-major axis, but random true anomalies, longitudes of perihelion, and ascending node. The dust number densities along the line of sight are largest along the edge of the torus which generates enhancements in the intensity curve. Figure on the left from [93], reproduced by permission of the AAS; Figure on the right courtesy of Masateru Ishiguro, Seoul National University, adapted from [91].

etary system as sketched in Figure (11). The interstellar dust has different trajectories from the solar system dust (Figure 12) and in in-situ measurements can be distinguished from the planetary system dust, when its velocity is larger than escape velocity and its direction of motion is similar to that of the neutral interstellar gas.The trajectories of the large interstellar dust particles in the heliosphere are shaped by repelling solar radiation pressure and attracting solar gravity force. The flux of smaller interstellar dust is more strongly influenced by Lorentz force and modulated in and around the heliosphere (see Section 5.3). Consequently, the interstellar dust particles that are identified with the in-situ instruments are at the upper end of the interstellar dust mass or size distribution [141].

The discussion of the Zodiacal brightness observations above has shown an analysis [211] ascribing it to a combination of asteroidal, cometary and interstellar dust in the solar system (see Figure 3). Indeed, the studies of the interplanetary dust with different methods can lead to quite different estimates of the dust cloud composition. Table 2 that compares some of these results is taken from a recent study that uses orbital information derived from the Dopplershift in the Fraunhoferlines of the Zodiacal light brightness [90]. The other estimates listed consider: the observation of different cratering rates on targets with different properties [245], the analyses of the shape of impact craters [22, 227, 46], the spatial shape of the dust cloud as seen in different Zodiacal light observations [135, 59, 185], and the analyses of asteroidal dust bands [61, 37, 38, 239, 178]. It is still surprising that studies often suggest the collected meteorites seem to originate exclusively from asteroids [86] and the observed meteors exclusively from comets [25].

Table 2: The fraction of dust from asteroids, comets and trans-Neptunian objects estimated from different observations. The estimate marked (*) refers to fragments from the asteroid families Karin and Veritas only. Table adapted from [90].

	Fraction of dust from			
Observations used	asteroids	comets	trans-Nept.	References
Cratering rates		0.75		[245]
Cloud shape (IRAS)		0.67 - 075		[135]
Cloud shape (COBE)	0.30	0.36	0.34	[59, 185]
Dust bands	> 0.3			[61, 37, 239]
Dust bands	most			[38]
Shape of microcaters	> 0.7			[22, 227, 46]
Dust bands (IRAS)	0.05 - 0.09*	hight speed		[178]
Doppler shifts	0.3 - 0.5	0.4 -0.7	< 0.1	[90]

4. Dust interactions in space

4.1. Basics of dust charging

Charging processes have been addressed by a number of authors in various contexts [217], [52], [175], [231], [45], [57], [233], [159]. This section will focus on the basics of the dust charging processes at work in the solar system, from the Earth's lower ionosphere to the solar wind and planetary magnetospheres. But even for these cases the parameters that influence dust charging, plasma density, temperature, and illumination, differ by many orders of magnitude. Dust grains charge by collecting and emitting charged particles, which changes the net charge and electrostatic potential, which in turn changes the fluxes of incoming and outgoing particles, until an equilibrium is reached when the electrical currents balance each other.
The main charging processes in the solar system are due to:

- impacts of electrons and ions which transfer their charge to the grain; the sticking probability is generally close to unity (except for nanograins in very cold or very hot plasmas), but energetic particles produce secondary emission;
- photoelectron emission induced by solar photons of energy greater than the work function of the grain material.

Before considering these processes in more detail, it is helpful to consider two special cases: the photoelectron emission being negligible and the the photoelectron emission being predominant.

Assume first that photoelectron emission is negligible, so that the charging is determined by ambient electron and ion fluxes (Figure 15 a). This is generally the case in dense planetary ionospheres [26], dense cometary environments [167], and plasma disks of outer planetary magnetospheres [53]. Because of their much smaller mass, electrons move much faster than ions at same temperature and in order to achieve quasi-neutrality the

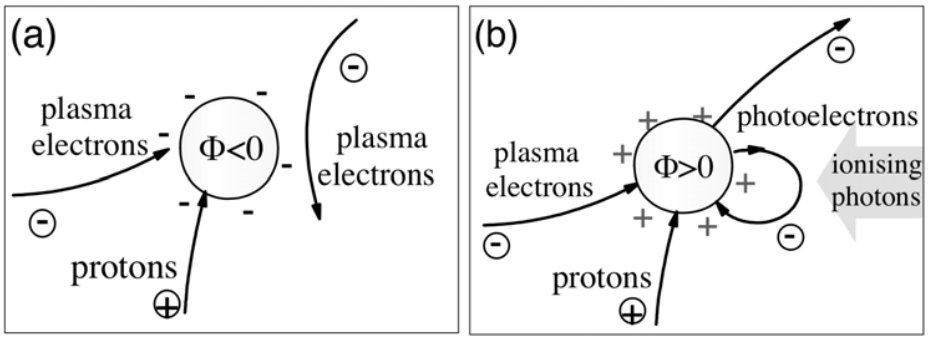

Figure 15: A dust grain impacted by plasma electrons and ions charges negatively because of the larger mobility of electrons; the charging continues until the grain's charge repels enough electrons to make the net current vanish (a). When the photoelectron flux from an uncharged grain exceeds the incoming electron flux, the grain charges positively until it traps enough photoelectrons to make the net current vanish (b). Figure adapted from [151].

charge number densities are generally similar. Hence the electron flux far exceeds the ion flux, so that the grain charges negatively. The accumulated negative charge then repels the incoming electrons, thereby reducing their collected flux. An equilibrium is reached when the grain's charge repels sufficiently the electrons so that their flux balances that of positive ions. For doing so, the grain's electrostatic potential Φ must ensure that the potential energy $-e\Phi$ outweighs (but not too much) the kinetic energy of the plasma electrons. We deduce that grains charge to a negative potential roughly equal (in V) to a few times the ambient electron temperature (in eV).

Consider now the case that photoemission dominates the charging (Figure 15 b). This is generally so in the solar wind. Since the grain ejects more photoelectrons than it collects ambient electrons (neglecting the smaller ion flux), its charges positively. This continues until the accumulated positive charge binds sufficiently the photoelectrons to reduce their escaping flux so that it balances the flux of incoming solar wind electrons. For doing so, the grain's potential must provide the photoelectrons with a potential energy $-e\Phi$ that outweighs (but not too much) their typical kinetic energy. Therefore a sunlit grain charges to a positive potential equal (in eV) to a few times the photoelectron temperature of a few eV.

The more detailed considerations below are based, for simplicity, on the assumption that the grains are macroscopic spheres. In practice this yields correct results for a non-spherical macroscopic grain if one assumes an effective radius $\sim (3\mathcal{V}/4\pi)^{1/3}$ for a grain of volume $\mathcal{V}$, provided that the length-to-diameter ratio is smaller than about ten. The charge may be much greater for long rods and fluffy grains [6]. Discussions in Section 4.5 will also show that the main results are expected to hold down to the molecular scales.

The small size of dust grains further simplifies the problem. First, since they are much smaller than the gyroradii of the plasma particles, one can neglect the Lorentz force on the plasma particles when calculating the currents. Second, since the dust grains are generally much smaller than both the collisional free path and the Debye length

$$L_D = \left(\epsilon_0 k_B T/ne^2\right)^{1/2} \tag{3}$$

of the plasma (of density n and temperature T), one can assume that the collected fluxes are determined by the particle orbital motions without intervening collisions or barriers of potential (Section4.2).

Two further scales enter the problem: the distance between grains $\sim n_d^{-1/3}$ (n_d being the grain number density), and the plasma Landau radius

$$r_L = e^2/(4\pi\epsilon_0 k_B T). \tag{4}$$

The Landau radius is the distance at which the mutual electrostatic energy of two plasma electrons $e^2/4\pi\epsilon_0 r_L$ equals their thermal energy $\sim k_B T$. The Landau radius is generally much greater than the grains' radius, so that one can neglect the polarization of the dust grain by the approaching electrons or ions. This is not so, however, for nanodust in extremely cold environments, as e.g. the Earth's mesosphere, with interesting applications (Section 6.2.2); we will discuss this case below (Section 4.5). Furthermore, in this case, the charge is so small that its quantization must be taken into account (Section 4.6).

The inter grain distance is generally much greater than the plasma Debye length, so that the charge on grains can be calculated as if they were independent of each other. The electric charge carried by a dust grain of radius a can then be deduced by approximating it by a spherical capacitor of capacitance $C = 4\pi\epsilon_0 a$, whence

$$q_d \simeq 4\pi\epsilon_0 a\Phi \tag{5}$$

for $a \gg r_L$. Since we have seen that $\Phi \sim k_B T/e$ where T is the temperature of the particles that dominate the charging, the grain charge state is then given in order of magnitude by $q_d/e \sim a/r_L$.

The charging time scale is then $\tau \simeq C\left(4\pi a^2\, e\, dN/d\Phi\right)^{-1}$ where N is the flux of the particles that dominate the charging [165]. The considerations below will show that $dN/d\Phi \simeq Ne/k_B T$, which yields the grain charging time scale $\tau \simeq (4\pi a r_L N)^{-1}$.

When the grains are not independent, they may lie within the Debye sphere of each other, and furthermore the grains' charge density becomes significant compared to those of the ambient plasma particles, which modifies them. This case will be shortly discussed in Section (4.7). Finally, for a very small grain, the electrostatic field produced by its charge may induce particle emission from its surface and can also make the grain explode. This will be considered in Section (4.8).

4.2. Charging by impacts of electrons and ions

The random flux of particles having an isotropic velocity distribution of number density n and mean speed $\langle v\rangle$ on an uncharged surface is

$$N_0 = n\langle v\rangle/4 \tag{6}$$

where the factor $1/4$ arises because for a given infinitesimal surface element, half of the particles are coming from one side and their average perpendicular velocity is $\langle v\rangle/2$. At local equilibrium of temperature T, the particle velocity distribution is a Maxwellian, so that the mean speed of particles of mass m and the random flux are respectively

$$\langle v\rangle = (8k_B T/\pi m)^{1/2} \tag{7}$$

$$N_0 = n(k_B T/2\pi m)^{1/2} \tag{8}$$

The flux is modified when the dust surface is charged at a potential Φ with respect to the unperturbed plasma. Consider electrons and singly charged positive ions. The charges having the same sign as Φ are repelled, and only those of initial kinetic energy greater than $|e\Phi|$ can reach the surface, so that the flux of repelled particles of temperature T is

$$N = N_0 \exp(-|e\Phi|/k_B T) \qquad \text{Repelled particles} \tag{9}$$

$$= N_0 e^{-|Z|r_L/a} \qquad Z = q_d/e \tag{10}$$

where we have substituted (Eq. 5) and (Eq. 4).

On the other hand, the charges of sign opposite to that of Φ are attracted, and in that case, the result depends on the geometry of the collecting surface, as does the Debye shielding [162]. Consider first particles of mass m, charge $\pm e$, and speed v, arriving isotropically from the unperturbed plasma at large distances. The trajectories are bent towards the grain by the attracting potential, so that the effective radius for particle collection is increased. Since the grain is much smaller than the plasma Debye length and the particle mean free paths, there are no intervening barriers of effective potential nor collisions, and at all energies there are trajectories coming from infinity and grazing the surface of the grain (the so-called "orbit-limited" condition [119]). In that case, the impact parameter p of the trajectory which just barely grazes the sphere of radius a defines the effective radius of collection of the particles. In spherical geometry, conservation of angular momentum and energy yields

$$p^2 = a^2(1 + 2|e\Phi|/mv^2). \tag{11}$$

This means that the grain has an effective radius increased by the factor $(1+2|e\Phi|/mv^2)$, so that the flux per grain unit surface becomes

$$N_v = (nv/4)(1 + 2|e\Phi|/mv^2). \tag{12}$$

This holds for attracted particles of number density n and speed v in the unperturbed plasma. This result is easily generalized to any isotropic particle velocity distribution, by averaging the flux (Eq. 12) over speeds, which yields

$$N = \langle N_v \rangle = n(\langle v \rangle/4 + |e\Phi|\langle 1/v \rangle/2m). \tag{13}$$

With a Maxwellian velocity distribution of temperature T, $\langle v \rangle$ is given by (Eq. 7) and

$$\langle 1/v \rangle = \langle v \rangle/2k_B T. \tag{14}$$

Substituting the averages (Eq. 7) and (Eq. 14) in the flux (Eq. 13) and using the expression (Eq. 6) of N_0 yields the flux

$$N = N_0(1 + |e\Phi|/k_B T) \qquad \text{Attracted particles} \tag{15}$$

$$= N_0(1 + |Z|r_L/a) \qquad Z = q_d/e. \tag{16}$$

It is illustrative to apply these results to the simple case of a plasma made of n electrons and n ions per unit volume, of respective charge $-e$ and e, and respective mass m_e and m_i,

with Maxwellian velocity distributions of respective temperatures T_e and T_i. The fluxes of electrons and ions on an uncharged surface (respectively N_{0e} and N_{0i}) are obtained by substituting the appropriate mass and temperature in the random flux (Eq. 8). Hence the flux of the (less massive) electrons outweighs the ion flux by a large factor, so that the grain charges negatively, repelling the electrons and attracting the positive ions. The fluxes of (repelled) electrons and (attracted) ions are then obtained from respectively (Eq. 9) and (Eq. 15) with the appropriate mass and temperature. At equilibrium, $N_e = N_i$, so that the grain's potential Φ is given by

$$e\Phi/k_B T_e = -\ln\left[(N_{0e}/N_{0i})/\left(1 - e\Phi/k_B T_i\right)\right] \tag{17}$$

with $N_{0e}/N_{0i} = (m_i T_e/m_e T_i)^{1/2}$. With one singly charged ion species of mass respectively m_p (the proton mass) and $30m_p$ and temperature $T_i \simeq T_e \simeq T$, (Eq. 17) yields the grain potential $\Phi = -\eta k_B T/e$ volts with $\eta \simeq 2.5$ and 3.9 respectively. In terms of the Landau radius (Eq. 4), the grain's charge (Eq. 5) is thus given in practice by

$$Z = q_d/e \simeq -\eta\, a/r_L \qquad 2.5 < \eta < 4 \tag{18}$$

If other charging processes are present as described below, the grain's potential may be positive. In that case, electrons (respectively positive ions) are attracted (respectively repelled), and the fluxes of electrons and ions are respectively deduced from (Eq. 15) and (Eq. 9), with the appropriate mass and temperature.

If the ambient particle velocity distributions are not Maxwellian, the flux of repelled particles is no longer given by (Eq. 9). It can be easily calculated from Liouville's theorem by noting that the velocity distribution at the grain's surface is translated in energy by $-|e\Phi|$, so that the repelled flux is deduced from the unperturbed energy distribution $f(E)$ as $N = (2\pi/m^2)\int_0^\infty f(E + |e\Phi|)EdE$. Calculating the flux of attracted particles requires more caution since the translation is now towards higher energies, which produces a hole in the distribution where orbits are not populated in the absence of collisions. In that case, it is simpler to derive the flux from (Eq. 13). This can be applied in planetary magnetospheres where one often observes Kappa velocity distributions [53], [164], [188], which have a greater proportion of high energy particles than a Maxwellian. In that case, the (repelled) electron flux is significantly increased since there are more particles of energy exceeding $|e\Phi|$. On the other hand, the (attracted) ion flux changes much less because one sees from (Eq. 13) that it depends only of low-order moments. Hence the grain's potential becomes more negative, as confirmed by detailed calculations [210]. The highest potentials are obtained in the regions of planetary magnetospheres shadowed by the planet, and can reach several tens of keV [53].

The above expressions neglect the grains' motion. This is often justified in the solar system, because the grains' velocity is generally much smaller than the thermal speeds of those ambient particles that contribute significantly to the charge fluxes. This may not be so in cold dense regions of planetary magnetospheres where the ion flux plays an important role in the charging when the dust-to-plasma relative velocity is not small compared to the ion thermal speed. In that case, the ion flux is modified (see e.g. [231]).

4.3. Photoelectron emission

In the interplanetary medium and in dilute regions of planetary magnetospheres, the dominating charge flux is generally due to photoemission produced by solar photons of energy

exceeding the work function of the grain material. For most bulk materials, the yield, i.e. the number of ejected photoelectrons per absorbed photon, becomes significant for photon energies above several eV, with a maximum yield in the range 0.05-0.5, depending on the physical and chemical structure of the material [47]. The photoelectron flux from an uncharged grain is found by integrating over the solar spectrum the product of the yield by the absorbed flux, which itself depends on the cross-section for photon absorption. The optical properties of small grains may be very different from that of bulk materials (see e.g. [107], [1]). Indeed, the photoemission yield is higher for small particles since, in order to be effective, the photoelectron excitation must occur closer to the surface than for bulk materials, so that the photoelectrons have a better chance to escape [229], [42]. On the other hand, the cross-section for photon absorption decreases significantly below the geometrical cross-section when the grain radius becomes smaller than about 10 nm ($\sim \lambda/2\pi$ where λ is the wavelength that contributes the most).

From the flux of solar ionising photons at the heliospheric distance $r_{\rm AU}$ (in astronomical units), which varies as $r_{\rm AU}^{-2}$, the photoelectron flux from an uncharged grain is approximately [60], [175]

$$N_{ph0} \simeq 0.5 \times 10^{14}\ \chi / r_{\rm AU}^2 \qquad \chi \sim 0.1 - 1 \tag{19}$$

per unit of the grain's surface $4\pi a^2$ (where we have taken into account that the projected sunlit area is one-quarter of the grain's surface area). The smaller value of χ corresponds to materials such as graphite or ice, the larger to silicates.

For most materials, the photoelectron velocity distribution can be approximated by a Maxwellian of temperature $T_{ph} \simeq$ 1-3 eV [60].

The flux (Eq. 19) also holds for a negatively charged grain since it repels the photoelectrons. On the other hand, as we already noted, the grain's charge becomes positive when the photoelectron flux dominates the charging. In that case the grain attracts the photoelectrons, and only those of kinetic energy exceeding $e\Phi$ (Φ being the grain's potential with respect to the distant unperturbed plasma) can escape, since the geometry is spherically symmetrical. Integrating over a Maxwellian photoelectron distribution of temperature T_{ph}, this yields

$$N_{ph} = N_{ph0}\,(1 + e\Phi/k_B T_{ph})\exp\left(-e\Phi/k_B T_{ph}\right) \qquad \Phi > 0 \tag{20}$$

This calculation is formally similar to the old Jeans [96] problem of the escape of atmospheres from the gravitational field of planets, and to the solar wind calculations in exospheric models [163], $e\Phi$ being in those cases replaced by the particle potential energy at the body's surface. Beware that (Eq. 20) is written incorrectly in a number of recent papers (e.g. [105] and many references therein), because they reproduce the one-dimensional escaping flux which is invalid for dust grains since they are generally much smaller than the (photoelectron and plasma) Debye lengths.

The grain electrostatic potential settles so that the photoelectron flux (Eq. 20) is balanced by the flux of incoming plasma electrons which is deduced from (Eq. 15) since they are attracted. When the photoelectron flux dominates the charging, one can generally neglect the ion flux which is smaller than the electron one, so that the grain equilibrium

potential can be approximated by

$$\Phi \simeq (k_B T_{ph}/e)\ \ln\left[\frac{0.5\times 10^{14}\ \chi/r_{\rm AU}^2}{n(k_B T_e/2\pi m_e)^{1/2}}\ \frac{1+e\Phi/k_B T_{ph}}{1+e\Phi/k_B T_e}\right] \quad (21)$$

Since the logarithm varies weakly with the parameters, this yields a potential of a few times the photoelectron temperature in eV, i.e. $\Phi \sim 1-10$ Volts. This holds when photoemission dominates the charging, in particular in the interplanetary medium, where (Eq. 21) yields a potential nearly independent on the heliocentric distance since both the photoelectron flux and the solar wind electron density vary as $r_{\rm AU}^{-2}$. It is also relevant for lunar dust on the Moon sunlit side, which is immersed in the solar wind, and also in dilute regions of planetary magnetospheres.

4.4. Secondary emission

When the electrons impacting the grains have an energy greater than the typical atomic binding energy $E_{Bohr} = m_e e^4/8\epsilon_0^2 h^2 \sim 10$ eV (where h is Planck's constant), they can excite secondary electrons, which are ejected with a typical energy of a few eV. Very energetic primary electrons excite electrons too deeply inside the grain to be able to escape, so that there is an optimum primary energy E_M for which the yield δ (the number of secondaries per primary) is maximum. In practice for bulk materials E_M is in the range of several hundreds eV, and the maximum yield is of order unity for metals and somewhat higher for insulators. However, the yield can still be higher when the grains are so small (<10 nm) that their size becomes comparable to the penetration depth of the primary electrons [44], [28], [2]. In the extreme case when the grain's size is smaller than the penetration depth, the primary electrons continue their trajectory within the grain and leave it after having produced secondaries, which compose a further current leaving the grain [44], [28].

In practice, electron secondary emission is significant only for primary electron energies between a few tens eV and several keV. Hence, it is generally negligible in the cold ionospheres of planets [26], and in cometary tails, where the plasma is rather cold [167]. Electron secondary emission may be significant for some materials in the solar wind, which contains a small but significant proportion of suprathermal electrons, and in planetary magnetospheres. Basic expressions for the electron flux with different velocity distributions for the incident electrons are given in [44], [193], [160], [28], based on secondary emission properties from [101], [218], [23], and in [107] (see also [57], but beware that Eqs.(3)-(4) in [57] are printed incorrectly; the correct original equations are to be found in [160]).

Secondary electron emission has two main consequences. First, by reducing the effective electron collected current, it makes the grains' electrostatic potential more positive. Second, when the electron velocity distribution differs significantly from a Maxwellian, with a higher proportion of suprathermal electrons as occurs in planetary magnetospheres, the grain potential may become multivalued. There are two stable equilibrium potentials of opposite signs for a given grain in a given environment; therefore an infinitesimal variation in ambient plasma properties can yield jumps in grain's potential, so that the grain's charge depends on its history, and similar grains in similar environments can have charges

of opposite signs [160]. We do not address here the secondary emission induced by ions, which can generally be neglected to calculate grain charging in space.

Figure (16) shows the calculated surface charge for silicate and graphite dust particles in the interplanetary medium taking into account photo ionisation and the solar wind impact. The different response of the particles to the variable solar wind conditions reflect the influence of secondary electron emission. For small particles other effects are possibly also important.

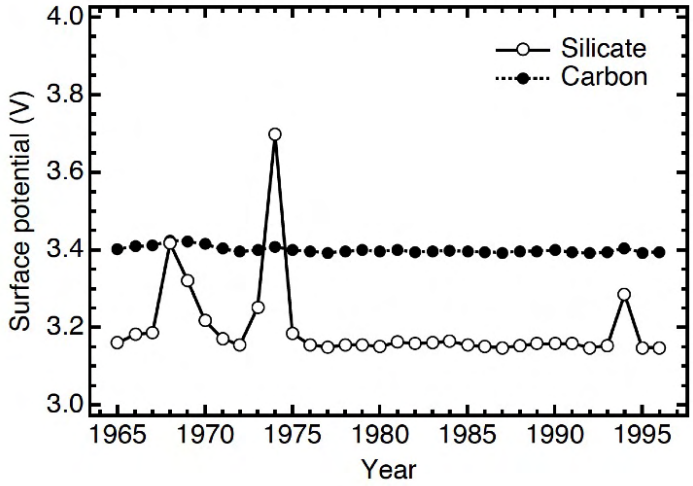

Figure 16: The surface charge of cosmic dust particles calculated for solar wind conditions during the years 1965 to 1996 close to Earth orbit, i.e. 1 AU distance from the Sun. The charge is shown in terms of surface potential versus infinity for silicate (open circles with solid line) and carbon particles (closed circles with dotted line) with mass 10^{-16} kg. Figure from [107], reproduced by permission of the AAS.

4.5. Grains' polarization

When the grain's size is not large compared to r_L, which can occur in very cold plasmas since (Eq. 4) yields $r_{L(\mathrm{nm})} \simeq 1.4/T_{\mathrm{eV}}$ two effects appear. First because of $q_d/e \sim a/r_L$ (Section 4.1), its number of charge units (Eq. 18) is not large. Second, the approaching plasma particles induce polarization charges on the grain, which can change significantly their collected fluxes, as first shown in the context of ion capture by aerosols [177]. Recall that r_L sets the scale of the collision cross-section of plasma particles since when two electrons approach each other closer than r_L, their mutual electrostatic energy exceeds their kinetic energy, so that their mutual repulsion strongly perturbs their trajectories [11]. A similar effect arises when plasma particles approach a dust grain closer than r_L, since the mutual electrostatic energy between the approaching particle and the charges induced on the grain exceeds the particle kinetic energy.

Consider an electric charge q approaching at distance r from the centre of a spherical dust grain of radius a carrying the electric charge q_d. The charge q is subjected to an electrostatic field that can be derived from the potential [95]

$$\Phi(r) = \frac{1}{4\pi\epsilon_0 a}\left[\frac{q_d}{x} - \frac{q}{2x^2(x^2-1)}\right] \qquad x = r/a \tag{22}$$

The first term is the Coulomb potential of the grain's charge q_d, the second stems from the image induced by the approaching charge q. This expression, which assumes that the grain behaves as a conducting sphere, is nevertheless a good approximation for dielectric grains of appreciable dielectric constant [45]. Equation (22) has two interesting consequences. First, in the limit $a \to 0$ ($x \gg 1$) the image term is the potential of a dipole moment $p = qa^3/2r^2$. Since the Coulomb field of the approaching particle with charge q is $E_0 = q/4\pi\epsilon_0 r^2$, this corresponds to an equivalent polarisability $\alpha = p/\epsilon_0 E_0 = 2\pi a^3$. This polarisability is close to that of a large molecule of similar size, which suggests that these calculations are expected to be a reasonable approximation down to the molecular regime.

Second, for particles that are repelled at large distances ($qq_d > 0$), the potential (Eq. 22) has a maximum at r_0 given by

$$2x_0^2 - 1 = (q_d/q)\; x_0(x_0^2 - 1)^2 \qquad x_0 = r_0/a \tag{23}$$

For singly charged grains and (repelled) particles, i.e. $Z = q_d/q = 1$, (Eq. 23) yields $x_0 \simeq 1.62$, whereas for $Z \to +\infty$ we have $x_0 = 1 + 0.5Z^{-1/2}$. At the maximum r_0 of the barrier of potential, the potential is

$$\Phi(r_0) = \frac{q_d}{4\pi\epsilon_0 a x_0}\left[1 - \frac{q/q_d}{2x_0(x_0^2-1)}\right] \tag{24}$$

which can be approximated by (see [45])

$$\Phi(r_0) \simeq \frac{q_d}{4\pi\epsilon_0 a}\;\frac{1}{1+Z^{-1/2}} \qquad Z = q_d/q > 0 \tag{25}$$

As soon as the particles come closer than the distance r_0 where the force changes of sign, they become attracted. Hence the effective collection radius is increased by the factor y_0 with $y_0 \simeq x_0$ when $x_0 \gg 1$ since in that case the incomig particles are weakly repelled outwards r_0. Furthermore, since only particles of energy at least equal to $\Phi(r_0)$ can reach this distance, the flux of repelled particles with a Maxwellian distribution of temperature T is given by (Eq. 9), substituting $q\Phi(r_0)$ obtained from (Eq. 25) instead of $e\Phi$ and multiplying by the factor y_0^2, i.e.

$$N = N_0 y_0^2 \exp(-|q\Phi(r_0)|/k_B T) \qquad \text{Repelled particles} \tag{26}$$

$$\simeq N_0\left[1 + (3|Z| + 4a/r_L)^{-1/2}\right]^2 \exp - \left(\frac{|Z| r_L/a}{1+|Z|^{-1/2}}\right) \qquad Z = q_d/e \tag{27}$$

where we have substituted (Eq. 25) and an approximation of y_0 derived by [45] to deduce (Eq.27), and assumed $q = \pm e$. Comparing with (Eq.10), one sees that the polarization increases the flux of repelled particles by the factor $y_0^2 \exp[(r_L/a)|Z|/(1+|Z|^{1/2})]$. For $|Z| = 1$ and $a/r_L \ll 1$, this factor $\simeq 2.6 \times e^{r_L/2a}$, which can be quite large for very small grains.

Consider now uncharged grains ($q_d = 0$). The polarization charges attract the incoming plasma particles, making their flux greater than the random flux (Eq.8). Consider as in Section (4.2) particles of mass m, charge $\pm e$, and speed v, arriving isotropically from large distances. They are subjected to the electrostatic potential (Eq.22) with $q_d = 0$.

The impact parameter p of the trajectory which barely grazes a sphere of radius r is given by (Eq.11), replacing a by r and Φ by $\Phi(r)$, whence

$$p^2/a^2 = x^2 + x_{Lv}/[2(x^2-1)] \qquad x = r/a \tag{28}$$

$$\text{where} \qquad x_{Lv} = [e^2/(4\pi\epsilon_0 m v^2/2)]/a \tag{29}$$

is the normalized Landau radius of the particles of speed v. Therefore $dp/dx = 0$ for $(x^2-1)^2 = x_{Lv}/2$ and p has a minimum given by

$$p_{min}^2/a^2 = 1 + \sqrt{2x_{Lv}} \tag{30}$$

The flux onto the grain is therefore the random flux $nv/4$ times the factor (Eq.30), i.e., using (Eq.29)

$$N_v = n\left[v + e\left(\pi\epsilon_0 m a\right)^{-1/2}\right]/4 \tag{31}$$

This result, which holds for particles arriving isotropically with density n and speed v, is easily generalized to a Maxwellian of temperature T. In that case the second term in the bracket of (Eq.31) is equal to $(\pi r_L/2a)^{1/2}\langle v\rangle$, where the mean speed $\langle v\rangle$ is given by (Eq.7), so that averaging (Eq.31) over the speeds yields the flux

$$N = N_0\left[1 + (\pi r_L/2a)^{1/2}\right] \qquad \text{uncharged grain} \tag{32}$$

with N_0 given by (Eq.8) and r_L given by (Eq.4). Therefore, the polarization increases the flux onto uncharged grains by the factor $\left[1 + (\pi r_L/2a)^{1/2}\right]$.

Finally, consider attracted particles ($qq_d < 0$). The calculation is much more complicated because the focusing has two causes: first, the field of the grain's charge $q_d = Ze$ considered in Section (4.2) which yields the flux (Eq.16) in the absence of polarization and acts far from the grain; second, the image contribution which yields the flux (Eq.32) when $q_d = 0$ and acts at short range. By comparing fluxes on respectively charged grains (Eq.16) and uncharged grains (Eq.32), one sees that the grain charge often has a stronger effect than the image charge, so that the flux of attracted particles for a Maxwellian distribution at temperature T is approximately given by Eq.(16).

These effects have some influence on the grain charge and on the time scales for charing. For grains' sizes comparable to or smaller than r_L, the flux of ambient charged particles increases whatever the grain's charge (attracting, repelling or neutral), so that the charging time scales decrease. Furthermore, we have seen that in the absence of photo and secondary emission, and when the polarization is negligible, i.e. when $a/r_L \gg 1$, the grain's charge (Eq.18) is proportional to its size. For smaller grains, the polarization changes the fluxes, and when the grain is so small than it tends to carry only one or zero charge unit, the state $Z = -1$ is favoured over the state $Z = 0$ [97], since the probability that a $Z = 0$ grain collects an electron is much higher than the probability that either a $Z = 0$ or a $Z = -1$ grain collects an ion, because of the much smaller random flux of ions (since $m_i \gg m_e$). These calculations, however, require a statistical treatment of the grain charge distribution as discussed below.

4.6. Charge probability distribution

Let $f(Z)$ be the probability that a grain carries the charge $q_d = Ze$. This charge increases by collecting positive ions or emitting photoelectrons, and decreases by collecting electrons (in this Section we do not consider secondary emission because these calculations are relevant in cold plasmas where this effect is negligible). Under stationary conditions, with singly charged plasma ions, the detailed balance equation is [45]

$$f(Z)\left[N_i(Z) + N_{ph}(Z)\right] = f(Z+1)N_e(Z+1) \tag{33}$$

which is equivalent to a more complicated recurrence relation used by [194]. When photoemission is negligible, this yields the simple recurrence relation

$$f(Z)/f(Z+1) = N_e(Z+1)/N_i(Z) \tag{34}$$

which can be solved by using $\sum_{-\infty}^{+\infty} f(Z) = 1$. In that case, for small grains the probability is concentrated on the states $Z = 0$ and -1. Applying (Eq. 32) to a $Z = 0$ grain collecting electrons and (Eq.16) to a $Z = -1$ grain collecting (attracted) positive ions of temperature T, we have

$$\frac{f(-1)}{f(0)} \simeq \left(\frac{m_i}{m_e}\right)^{1/2} \frac{1 + (\pi r_L/2a)^{1/2}}{(1 + r_L/a)}. \tag{35}$$

In the limit $a \ll r_L$, this yields $f(-1)/f(0) \sim (\pi m_i a/8m_e r_L)^{1/2}$, which is generally much greater than unity in the solar system, so that the mean charge state is expected to be $Z \simeq -1$ in this case.

In practice, recalling (Eq.18), one can therefore approximate the grain charge state $Z = q_d/e$ at equilibrium in the absence of photo and secondary emission by

$$Z \simeq -\left(1 + \eta\, a/r_L\right) \tag{36}$$

with η varying from 2.5 to 4 when the ion mass varies from m_p to $30m_p$. This approximation (Eq.36) is rather close to the numerical results found in the solar system (see e.g. in [97], [194]). A more accurate approximation should be used in still colder environments found in the interstellar medium [45] or when a large concentration of dust affects the plasma so that the electron and ion number densities are no longer equal (Section 4.7). These calculations have important implications for dust charging in the Earth's mesosphere, which is the coldest place in the Earth's ionosphere (Sect 6.2.2).

4.7. "Dust in plasma" versus "dusty plasma"

The above calculations hold when the grains' charges do not influence each other nor the plasma. For the grains not to influence each other, they should lie outside their mutual regions of electrostatic influence set by their Debye spheres. Therefore their number density n_d should be small enough to ensure that their separation $\simeq (3/4\pi)^{1/3} n_d^{-1/3} > 2L_D$. Furthermore, for the grains not to influence the plasma, their charge density $n_d q_d$ should be much smaller than the charge density of plasma charges, i.e. $n_d|Z| \ll n$.

Consider the case when photo and secondary emission as well as grains' polarization are negligible. In that case, if the grains do not influence each other nor the plasma, their

charge is deduced from (Eq.18) as $Z = q_d/e \simeq -\eta a/r_L$. Therefore the ratio of the charge carried by the grains to that carried by the plasma electrons is $n_d|Z|/n \simeq \eta(n_d/n)(a/r_L)$. From the expression (Eq.4) of r_L, this can be rewritten as $4\pi\eta n_d a L_D^2$, i.e., η (of order of magnitude unity) times the non-dimensional parameter

$$P = 4\pi n_d a L_D^2 \tag{37}$$

$$< \left(2n_d^{1/3} L_D\right)^2 \tag{38}$$

where (Eq.38) holds because the grain separation is greater than the grain diameter.

Therefore, the unperturbed grain-to-electrons charge ratio is expected to be a critical non-dimensional parameter for the electrostatics of a dusty plasma. Indeed, if $P > 1$, not only is the grains' charge expected to disturb the plasma quasi-neutrality, but from (Eq.38) the grains' Debye spheres overlap, which changes the grains charge.

More detailed calculations [232] (see also [56], [80]) confirm this estimate. When $P < 1$, the plasma electron and ion number densities remain equal and the grain's charge is roughly that of independent grains. However, when $P > 1$, plasma electrons tend to be depleted since many of them rest on the grain's surface. Therefore, the grains need not be as negatively charged as when they are independent to equilibrate the electron and ion fluxes on their surface. This effect is somewhat reduced (but not suppressed) by the fact that when the grains separation becomes smaller than L_D but is not much larger than the grains' radius, the neighbouring grains increase the grain-to-plasma capacitance so that (Eq.5) no longer holds [232]. Hence when $P > 1$, the grain charge is reduced and the plasma densities change, so that we no longer have "dust in plasma", but rather a dusty plasma". In the extreme case when $P \gg 1$, most plasma electrons are trapped on the grains, whose charge density must compensate that of ions, so that

$$Z = q_d/e \sim -n/n_d \qquad \text{for } P \gg 1 \tag{39}$$

which is smaller by the factor $\eta\, P$ than the charge (Eq. 18) of independent grains.

Finally, in some cases, the grains also decrease the plasma density by constituting a plasma and photon sink [194]. This happens when the electron sink due to their capture by grains $\sim 4\pi a^2 n_d \times n\,(k_B T/2\pi m_e)^{1/2}$ exceeds the electron production or recombination rate (and/or alternatively if the photon absorption by grains exceeds that of atoms. This may happen e.g. in the cold Earth lower ionosphere (Section6.2.2).

4.8. Field emission and electrostatic disruption

For very small grains, the surface electrostatic field may become very large so that the grain may emit electrons or ions (see [44]).

Small negatively charged grains can eject electrons because the surface electric field E deforms the potential barrier at the surface (which normally has a height of the order of the work function W) so that it acquires a width $\sim W/|E|$. This enables the electrons below the surface to tunnel efficiently if their wavelength exceeds this width. In practice this process becomes efficient when $|E| > 10^9$ V/m [58]. An ejected electron near the surface of a grain of charge $Ze < 0$ will be subjected to the field amplitude $|E| \simeq (Z+1)e/4\pi\epsilon_0 a^2$.

Hence the condition $|E| < 10^9$ V/m for electron field emission not to occur limits the grain charge state to [45]

$$Z > -\left(1 + 0.7\, a_{nm}^2\right) \tag{40}$$

Comparing with (Eq.36), one sees that electron field emission limits the negative grain charge when $a_{nm} < \eta\, T_{eV}$ (where $\eta \sim 2.5 - 4$, depending on the ion mass). In practice this might occur for nanodust in outer planetary magnetospheres and near comets (see [158] but beware that in this paper and several references therein, the limit for electron field emission is used incorrectly whatever the charge sign).

On the other hand, for positively charged grains, field emission can occur only for ions. This process becomes efficient when the surface field $E > 3 \times 10^{10}$ V/m [176]. Thus positive grains can support much higher charges than negative ones. With the same reasoning as above, one sees that this limits the grain charge to

$$Z < 1 + 20\, a_{nm}^2 \tag{41}$$

When photoemission dominates dust grains are in general positively charged (Section4.3) and in that case $\Phi \sim$ 1-10 V in the solar radiation. Considering the grain charges from Eq.5 together with Eq.41 one can deduce that ion field emission occurs in the interplanetary medium only for grains' radius smaller than a fraction of nm, which corresponds to the molecular regime.

The high electrostatic field at the surface of a small grain has another consequence. It can break the grain when the corresponding electrostatic stress $\epsilon_0(\Phi/a)^2$ exceeds the maximum tensile strength against fracture S_{max}. The grains' tensile strength is very dependent on their composition, structure and size. Extreme bonds may be set by fluffy cometary material ($S_{max} \sim 10^5$ N m^{-2}) and polycrystalline bulk solids or tektites ($S_{max} \sim 10^9$ N m^{-2}). Setting $S_{max} = \gamma \times 10^9$ N m^{-2}, we deduce that electrostatic disruption occurs if the grain's potential exceeds $\Phi_{max} = 10\, \gamma^{1/2}\, a_{nm}$, whence, from (Eq.5)

$$|Z_{max}| = 7 \times \gamma^{1/2}\, a_{nm}^2 \quad \text{Electrostatic disruption} \tag{42}$$

Recalling the field emission limits found above, we deduce that electrostatic disruption is not expected to occur if $Z > 0$ whatever the value of γ, nor if [$Z < 0$ and $\gamma \geq 10^{-2}$] since the grain is discharged by field emission before reaching the critical potential.

4.9. Concluding remarks on dust interactions

Some of the interactions that play a role in other plasma environments are not, or only barely noticed in the solar wind. The photoelectron emission, for instance, also provides a source of electrons in the surrounding medium. Heating by photoelectrons is one of the processes that are discussed to explain the gas temperature in the the diffuse interstellar medium and for this mechanism the nanodust and the molecules are found to be most efficient [7]. The dust particles in the solar system are embedded in the high temperature solar wind, so that photo-electric heating is not relevant [133]. The presence of dust rather leads to cooling by the photoelectrons and by ions that charge-exchange and are decelerated when passing a dust particle and this process is more efficient for the nanodust than for larger particles. It was however found to be not particularly important for the solar wind [143, 145].

The dust destruction by sublimation and by neutral collisions can also release atoms and molecules into the ambient solar wind. A quantitative estimate showed that this somewhat influences the amount of the minor species in the solar wind [143].

This section has concentrated on the aspect of dust charging. Our knowledge of the dust charging is largely based on theory, using material parameters measured with large samples. Laboratory measurements at single dust particles are difficult (see e.g. [15]) and may in some cases reveal processes not considered yet. The direct dust charge measurements in space are difficult to achieve. The dust charging is likely to be among the most important dust interactions in the solar system. It is relevant for processes in the Earth atmosphere and for the acceleration of nanodust in the solar wind, both topics discussed in Section 6). But it is also generally important for the dynamics of dust in space.

5. Dust Dynamics in Space

In this section we discuss the effects of different forces acting on dust grains in the solar system and its immediate vicinity. We concentrate on the effects of the electromagnetic forces, and in particular on the recently obtained results for nanometer sized dust particles (the nanodust). For reviews of the overall plasma environment structure of the region considered see Holzer [84] and Zank [242].

5.1. The heliosphere and surroundings

The majority of the dust cloud of our planetary system is situated within heliosphere and a large fraction of the dust that is studied with observations is located within its inner part. The heliosphere, the region of space filled by the solar wind plasma and the solar magnetic field (see Section 3.1). It is separated from the local interstellar medium (the Local Cloud through which the Sun is moving) by a boundary surface called the heliopause. Since the solar wind outflow from the Sun is highly supersonic, before reaching the heliopause it must pass through a termination shock, where the flow is decelerated. This transition was confirmed by the Voyager spacecraft, which crossed the shock respectively at 94 AU (Voyager 1) and 84 AU (Voyager 2) from the Sun.

According to present models, the heliosphere has a comet-like shape with a blunt "nose" in the direction of the motion of the Sun relative to the interstellar medium and a long tail in the opposite direction (Figure 17). Voyager 1, now at ∼120 AU from the Sun, is presently thought to be approaching the heliopause in the "nose" region. The solar plasma near the boundary is rarified to about 0.002 particles/cm^3 [204]. The Local Cloud ionized plasma, with the density indirectly estimated at ∼0.06 cm^{-3} [51], flows around the heliopause, but the neutral atom component (∼0.2 cm^{-3} [51]) enters the heliosphere and the planetary system.

The solar magnetic field together with the solar wind determine the electromagnetic force acting on the grains. We shall refer to a simple model which was used by Czechowski and Mann [33]. It is defined as follows: The reference frame is nonrotating with the origin at the centre of the Sun. The angle θ of the spherical coordinate system (r,θ,ϕ) is the solar co-latitude.

Solar wind velocity $\mathbf{V}$ is radially directed and independent of distance: $\mathbf{V} = V\hat{\mathbf{e}}_r$ with slow solar wind (V=400 km/s) for latitudes within $\pm\bar{\Theta}$ from the solar equator and fast solar wind (V=800 km/s) elsewhere.

Solar magnetic field $\mathbf{B}$ has the form of the Parker spiral (3.1):

$$\mathbf{B} = \tilde{B}_r \frac{\hat{\mathbf{e}}_r - kr\hat{\mathbf{e}}_\phi}{(r/\bar{r})^2} \tag{43}$$

with $k = (\Omega/V)sin\theta$, $\Omega\equiv$solar rotation rate and $\tilde{B}_r$ the radial component of $\mathbf{B}$ at $r = \bar{r}$=1 AU. The values assumed in [33] are 3.5 nT in the slow and 4.5 nT in the fast wind region. Note that the radial and azimuthal components of $\mathbf{B}$ behave with distance as $B_r \propto 1/r^2$ and $B_\phi \propto 1/r$, respectively, and that B_θ=0.

The solar surface is divided into two hemispheres by the neutral line, taken in [33] to be a great circle tilted (by the angle $\bar{\Theta}$) relative to the solar equator plane. The field lines with footpoints in one of these hemispheres correspond to the opposite sign of $\mathbf{B}$ than those in the other. The regions of opposite field polarity are separated by the heliospheric current sheet stretching outwards from the neutral line and convected by the plasma flow. The case when the field in the northern hemisphere is incoming ($B_r < 0$) is denoted as the "focusing" orientation, since the electric field $-\mathbf{V}\times\mathbf{B}$ and the drift of the positively charged particles are then directed towards the current sheet.

The model provides a simple approximation to the solar wind and magnetic field (with time variations averaged out) in the region of supersonic solar wind, inwards from the termination shock. It is not applicable in the immediate vicinity of the Sun (few solar radii) where the plasma corotation becomes important. For a model of the grain dynamics (above the nanodust size) in this region see Krivov et al. [114].

The magnetic field in the Local Cloud is unrelated to the solar field. It is expected to be inclined at some angle respective to the direction of the solar motion relative to the cloud.

5.2. Equations

The equation of motion for a dust particle in the interplanetary space including the most important interaction terms can be written as

$$\frac{d\mathbf{v}}{dt} = \frac{q_d}{m}(\mathbf{v}-\mathbf{V})\times\mathbf{B} - \frac{GM_S}{r^2}\hat{\mathbf{e}}_r + \mathbf{F}_\gamma \tag{44}$$

where $\mathbf{v}$, q_d and m are the velocity, the charge and the mass of the dust grain, $\mathbf{V}$ is the plasma velocity, $\mathbf{B}$ the magnetic field, G the gravity constant, M_S the solar mass.

The first term is the electromagnetic force, which is equal to the Lorentz force in the local plasma rest frame where the electric field $-\mathbf{V}\times\mathbf{B}$ induced by the plasma flow vanishes. The intrinsic electric field is assumed to be absent in the plasma rest frame. $\mathbf{F}_\gamma$ stands for the radiative (Poynting-Robertson) force due to solar photons [192, 209, 19]:

$$\mathbf{F}_\gamma = \frac{GM_S}{r^2}\beta\left((1-\frac{v_r}{c})\hat{\mathbf{e}}_r - \frac{\mathbf{v}}{c}\right) \tag{45}$$

Here v_r the radial component of the dust velocity and β is the radiation pressure to gravity ratio:

$$\beta = \frac{\pi R_S^2}{GM_S cm} \int_0^\infty B_S(\lambda) C_{pr}(a, oc, \lambda) d\lambda, \tag{46}$$

where c is the speed of light, B_S the solar irradiance, C_{pr} radiation pressure cross section which depends on dust size, structure, and optical constants, oc of dust material, a the particle size and λ the wavelength and R_S is the radius of the Sun [148]. The maximum β-value for dust in the solar system is around 0.5 to 0.8 and corresponds to the size between 0.4 and 0.9 μm. For the grains considered here $\beta \sim 0.1$ is a reasonable estimate.

The velocity-independent radial part of radiation pressure force is called direct radiation pressure force, $\mathbf{F}_{\rm rad}$. The radiation force causes the Poynting-Robertson drag, resulting in reduction in the orbital energy and the angular momentum of the orbits of dust grains.

The forces due to ion or neutral atoms impacts on the grains are not included in Eq. 44. The solar wind impacts lead to the effect similar to (but weaker than) the Poynting-Robertson radiative term [169]). The friction caused by collisions with neutral atoms, although negligible in the inner solar system, may become relevant at larger distances [214].

The charge q_d of the dust grain fluctuates around the equilibrium value $\bar{q_d}$ which depends on the grain characteristics (material, size) but also on local conditions [107]: in result, $\bar{q_d}$ varies during the grain motion and the Eq. 44 must be supplemented by the charging equation

$$\frac{dq_d}{dt} = \sum_i j_i \tag{47}$$

where j_i are the rates of different charging processes. When charge fluctuations frequency is less or comparable to the gyrofrequency the charge q_d should be treated as stochastic variable.

Each of the terms present in Eq. 44 may become dominant for some range of the grain sizes. In the solar system the large grains (with the radius $s{\sim}1$ μm and larger) have their motion determined by the gravity force. The Poynting-Robertson force affects the long term evolution of their orbits, leading to their circularization and contraction of the orbital radius. The Poynting-Robertson contraction time of the orbital radius from r_0 to r is easily found to be $\sim (1/\beta)(400yrs)(r_0/1AU)^2(1-(r/r_0)^2)$. The Poynting-Robertson contraction speed for a circular orbit u_{PR} is proportional to $1/r$. This has an effect on the profile of the dust density distribution $n(r)$ in the circumsolar dust disk. If the Poynting-Robertson drag would dominate the inward transport of the dust, the conservation law $\nabla \cdot (n\mathbf{u}_{PR}) = 0$ would imply $n(r) \propto 1/r$. The observed distribution behaves as $n(r) \propto r^{-1.3}$.

The electromagnetic force, although substantially weaker than gravity for the large grains, can also affect their long time behaviour. This was investigated by Morfill and Grün [171] who found that the alternating polarity structure of the magnetic field leads to the stochastic spreading of the orbital inclination of the dust particles as they spiral towards the Sun due to the Poynting-Robertson drag.

Moving towards the smaller size, the radiation pressure (proportional to the area of the grain) becomes comparable to gravity ($\propto$ volume). Although the result depends on the optical properties of the grain material, the radiation pressure to gravity ratio β may exceed 1 for the grain sizes $s{\sim}0.1$ μm. The grains with high enough β ($\beta{>}0.5$ is sufficient for a grain starting with Keplerian orbital speed) are then expelled from the vicinity of the star, becoming β-meteoroids. For even smaller grains, the photon absorption rate ceases to be proportional to the grain area, because the absorption length becomes comparable to the grain size, and the value of β decreases.

The effect of the Lorentz force can be estimated using the gyrofrequency (the Larmor frequency) $\Omega_L \equiv q_d B/m$, the rigidity $R \equiv pc/q_d$ (with p the particle momentum) or the gyroradius (the Larmor radius) $R_L \equiv v'_\perp/\Omega_L$ where $v'_\perp$ is the grain speed perpendicular to the magnetic field in the plasma frame. With q_d/m in units e/m$_p$ and B in Tesla, $\Omega_L{\approx}$ q_d/m $\times 10^8$ ($\times$B radian/s).

Because of the velocity dependence, the strength of the Lorentz force depends on the initial motion of the charged grain relative to plasma. Since Ω_L is independent of the grain velocity, the knowledge of R_L or rigidity is important for making estimations.

When the gyroradius is much larger than the characteristic scale of variations of the magnetic field, the guiding centre approximation is applicable. The equation for the guiding centre motion along the magnetic field line is [181]

$$\frac{dv_\parallel^G}{dt} = g_\parallel - \mu\partial_S B + v_\parallel^G \mathbf{V}_\perp \cdot \partial_S \hat{\mathbf{b}} + \mathbf{V}_\perp \cdot (\mathbf{V}_\perp \cdot \nabla)\hat{\mathbf{b}} \tag{48}$$

where $v_\parallel^G$ is the parallel velocity of the guiding centre, $g_\parallel$ the parallel component of the gravity force, $\mathbf{V}_\perp$ the perpendicular component of the plasma velocity, $\mu \equiv |\mathbf{v}-\mathbf{V}|_\perp^2/2B$ the adiabatic invariant, S the distance along the field line and $\hat{\mathbf{b}} \equiv \mathbf{B}/B$. The derivative $\partial_S \equiv \hat{\mathbf{b}} \cdot \nabla$ is over the distance S along the magnetic field line. As in Eq. 44 we assume that the electric field vanishes in the plasma frame.

The guiding centre motion in the transverse direction is given by [181]

$$\mathbf{v}_\perp^G = \mathbf{V}_\perp + \mathbf{V}_D \tag{49}$$

where $\mathbf{V}_D$ is the drift velocity

$$\begin{aligned} \mathbf{V}_D \;=\; & \frac{1}{2}\frac{v'^2_\perp}{\Omega_L}\frac{\hat{\mathbf{b}}\times\nabla B}{B} + \frac{1}{\Omega_L}[-\hat{\mathbf{b}}\times\mathbf{g} \\ & + v_\parallel^2 \hat{\mathbf{b}}\times\partial_S\hat{\mathbf{b}} + v_\parallel \hat{\mathbf{b}}\times(\mathbf{V}_\perp\cdot\nabla)\hat{\mathbf{b}} + v_\parallel\hat{\mathbf{b}}\times\partial_S\mathbf{V}_\perp + \hat{\mathbf{b}}\times(\mathbf{V}_\perp\cdot\nabla)\mathbf{V}_\perp] \end{aligned} \tag{50}$$

In many situations of interest (smooth field, large Ω_L) $\mathbf{V}_D$ is small and the guiding centre stays close to the same magnetic field line.

5.3. Example: interstellar grains near the heliosphere

Consider the interstellar dust grains in the local interstellar cloud that encounter the heliopause. The velocity distribution of the dust grains in the interstellar medium is unknown and to our knowledge no detailed models were considered. If the grains move

initially together with the interstellar matter in the local cloud, then $v'_{\perp} = 0$ (the thermal velocity is negligible) and $R_L = 0$. The magnetic field in the local cloud may be ∼0.5 nT.

On approaching the forward part (the "nose") of the heliosphere the interstellar plasma flow must change direction to pass around the heliopause. The region where the flow is modified is called the outer heliosheath. The plasma velocity component in the initial flow direction must then change from the speed of the cloud relative to the Sun (V_C ∼20 km/s) to approximately zero over some distance L, probably of the order of 100 AU (the characteristic size of the heliosphere). The ratio L/V_C defines the characteristic time $\tau_f \sim 10^9$ s for the change of the flow. If the gyration time $T_L \equiv 2\pi/\Omega_L$ is much larger than τ_f the dust grain cannot adjust its motion to the plasma flow and will continue in the original direction, crossing the heliopause and entering into the heliosphere.

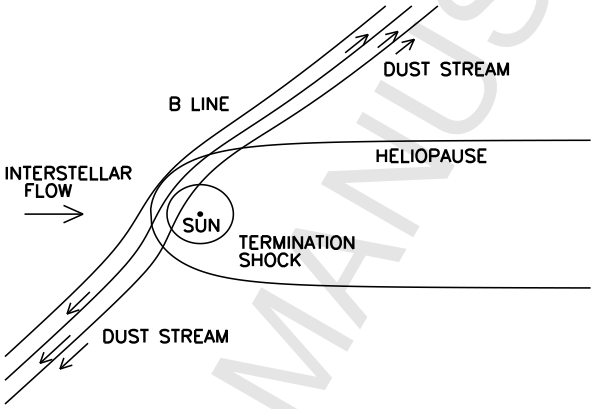

Figure 17: Development of streaming motion of the small (∼0.01 μm) interstellar grains that encounter the heliosphere. The grains stream away from the regions of higher magnetic field along the magnetic field line convected by the plasma flow bypassing the heliopause.

We now consider values of surface-charge-to-mass-ratio typical for the dust assuming $q_d/m \propto 1/a^2$ and the surface potential ∼2 V, since probably dust charges in the interstellar medium are lower than in the heliosphere [107]. For the cases of $q_d/m = 10^{-9}$, 10^{-7} and 10^{-5} e/m_p which correspond approximately to $a \sim 0.5$ μm, 0.05 μm and 0.005 μm dust grains, the values of T_L are $\sim 10^{11}$, 10^9 and 10^7 s, respectively, when assuming 0.5 nT for B. This implies that the interstellar grains of ∼0.5 μm radius decouple from the interstellar flow and enter the heliosphere, while the grains with $a \sim 0.005$ μm go around the heliopause with the interstellar flow. The $a \sim 0.05$ μm grains are the boundary case. Observations [64],[65],[122] and models [128],[134],[121],[31] confirm that the large interstellar grains can reach the inner solar system. The interstellar dust particles are suppressed below masses $\sim 10^{-16}$ kg or sizes ∼0.2 μm.

The motion of small grains (q_d/m ∼10^{-5} e/m$_p$) can be understood using the guiding center approximation. One result is that the grains approaching the heliopause may develop an ordered motion (streaming) away from the heliosphere [32] along the interstellar magnetic field lines (see Figure 17). This is due to the enhancement of the magnetic field strength in result of draping over the surface of the heliopause. The mirror force term

in Eq. 48 causes the streaming. Since the mirror term is proportional to the adiabatic invariant μ, the streaming develops only provided the grains acquire a big enough transverse velocity difference relative to plasma [32]). This can occur if the interstellar plasma passes through the bow shock in front of the heliopause: the dust grains cross the shock freely while the plasma flow is decelerated.

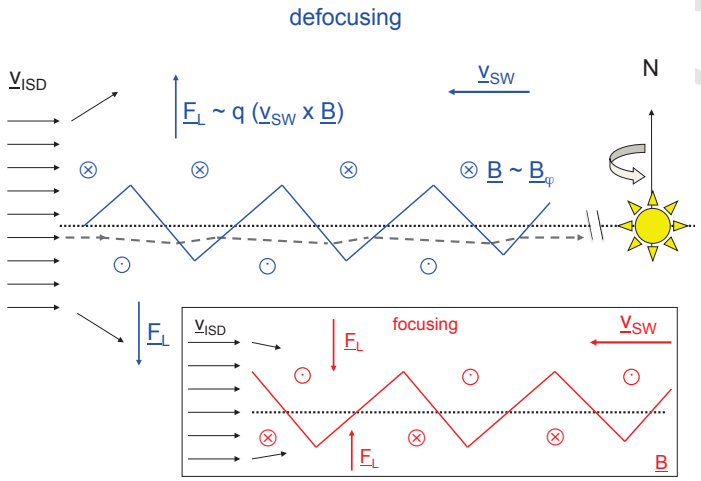

Figure 18: Interstellar dust (ISD) moving with velocity v_{ISD} into the heliosphere. The dust flux comes from the left and is parallel to the equatorial plane (dotted line), the magnetic field lines are perpendicular to the plane of the sketch diagram. The defocusing field configuration is shown in blue, the opposite (focusing) field configuration shown in red. The wavy current sheet is approximated with zigzag solid line, it separates the regions of opposite magnetic field polarity. The gray dashed line describes the path of a dust particle that enters the heliosphere close to the equatorial plane and through frequent crossing of the wavy current sheet avoids complete deflection [31]. Figure adapted from [141].

The grains which cross the heliopause (Figure 18) and enter into the heliosphere interact with the solar magnetic field and the solar plasma flow, which deflect the smaller size grains from their initial direction of motion and prevent them from reaching the inner solar system. This deflection can to some degree be suppressed by the sectored structure of the solar magnetic field originating from different polarity regions on the surface of the rotating Sun. The alternating field polarity in the sectors through which the grain is passing corresponds to deflection in alternating directions, so that the net effect is reduced [121], [31]. This effect illustrates the sensitivity of the small grain dynamics to the structure of the magnetic field. The models of the heliosphere aiming to describe the dust motion must therefore correctly account for this structure, a requirement difficult to achieve for numerical solutions. Another consequence of the field configuration is that, depending on solar cycle, the particles that enter the heliosphere are deflected either toward the current sheet, or away from it. This results in variations of a factor of 3 of the interstellar dust flux observed with Ulysses [121, 141].

5.4. Example: nanodust grains in the inner solar system

In the interplanetary space the Lorentz force dominates the nanodust dynamics. The presence of fast flowing solar wind, the magnetic field sector structure and the heliospheric

current sheet contribute to its effect.

The action of the electromagnetic force on the solar system dust grains was investigated among others by Morfill and Grün [171], [172], Hamilton et al. [72] and Krivov et al. [114] but the grain sizes they considered were above or at the upper boundary of the nanodust range. This section summarizes the results of a study by Czechowski and Mann [33, 34] based on a simple model of the solar wind presented above.

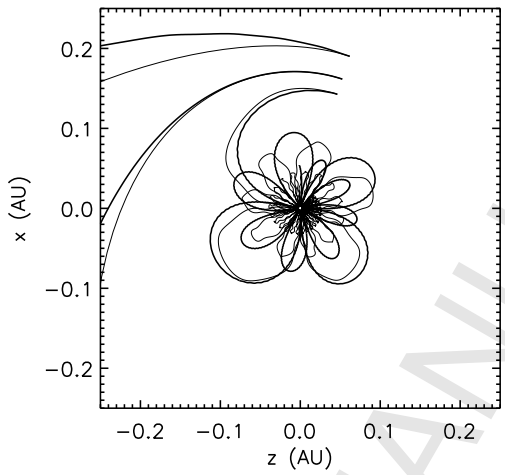

Figure 19: Trajectories (projected onto the ecliptic plane) of the grains with $q_d/\mathrm{m}=10^{-5}$ e/m$_p$ (thick lines) and $q_d/\mathrm{m}=10^{-6}$ e/m$_p$ (thin lines) released from circular orbits near the ecliptic with the radii 0.15, 0.17 and 0.2 AU.

The equation of motion is the Eq. 44 where the radiation pressure to gravity ratio is set to $\beta = 0.1$ for the nanodust particles. The grain electric charge q_d is taken to be a constant. The typical values of the charge to mass ratio q_d/m used in the study are 10^{-5}-10^{-4} e/m$_p$ which can be taken to correspond to the grain radii of ∼10 nm and ∼3 nm, respectively for the surface potential of ∼8 V.

The initial velocity of a freshly created nanodust particle is assumed to be equal to Keplerian velocity for a circular orbit. Most nanodust particles are expected to be created close to the Sun, where collisional fragmentation of larger dust grains or nanodust released from the comets are most likely to occur. The relative velocities of the fragments (few km/s) would then be significantly smaller than the orbital velocities of the parent bodies.

For a particle with $q_d/\mathrm{m}=10^{-4}$ e/m$_p$ (10^{-5} e/m$_p$) at the distance r=0.2 AU from the Sun Ω_L ∼7 10^{-4} (∼7 10^{-5}) radian/s and the initial Larmor radius $R_L \ll r$ implying that the guiding centre approximation may be applied (except for the effects of the current sheet: see below).

The results of the model calculations are as follows:

(1) Particles created close enough to the Sun are trapped in bound orbits. Figure (19) shows sample of trajectories of the nanodust created near the ecliptic plane at 0.15 AU, 0.17 AU and 0.2 AU from the Sun. The trajectories starting at 0.15 AU are trapped. The contraction of the orbits is caused by the Poynting-Robertson force, the effect of which is enhanced by small perihelium distance. Note also the similarity between the orbits for different q_d/m.

The trapping can be understood with the help of the guiding centre approximation. Evaluating the terms in the equation for the guiding centre motion along the magnetic field line [181] for the case of the Parker field in the vicinity of the Sun (where $kr \ll 1$) one obtains the equation for the radial component v_r^G of the guiding center velocity [33, 34]

$$\frac{v_r^G}{dt} = W(r) - k^2 (v_r^G)^2 \tag{51}$$

which, together with the equation for the radial coordinate of the guiding centre $dr^G/dt = v_r^G$, define a dynamical system in the (r^G, v_r^G) phase plane. $W(r)$ is given by

$$\begin{aligned} W(r) &= \frac{GM_S(1-\beta)}{r^2} + \frac{2\mu \tilde{B}_r \bar{r}^2}{r^3} + V^2 k^2 r \\ &= \frac{GM_S(1-\beta)}{r^2}\left[-1 + \frac{r_2}{r} + \left(\frac{r}{r_1}\right)^3\right] \end{aligned} \tag{52}$$

with $r_1 = (GM_S(1-\beta)/V^2k^2)^{1/3}$ and $r_2 = 2\mu\tilde{B}_r\bar{r}^2/GM_S(1-\beta)$ giving the approximate positions of the two fixed points of the dynamical system. Note that at $r = r_1$ the effective gravity force $GM_S(1-\beta)/r^2$ is equal to the "centrifugal" term V^2k^2r associated with the rotation of the magnetic field line (the term $+\mathbf{V}_\perp \cdot (\mathbf{V}_\perp \cdot \nabla)\hat{\mathbf{b}}$ in Eq.). At $r = r_2$ the effective gravity is balanced by the magnetic mirror force (Figure 20). The outer and the inner bounds on the trapped orbits are close to r_1 and r_2, respectively.

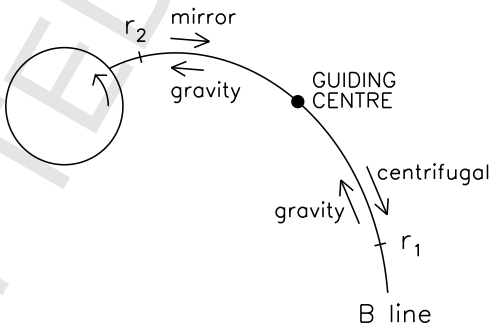

Figure 20: The mechanism of trapping of the nanodust particles in the vicinity of the Sun. The particle motion can be approximated as the guiding centre motion along the rotating magnetic field line. The outer boundary of the trapping region is near the point r_1 where the outward-directed centrifugal force associated with the rotation of the magnetic field line exceeds the gravity force. The inner boundary is near r_2 where the outward-directed magnetic mirror force balances gravity.

This simple analytical model is in good agreement with numerical solutions of the full equation of motion (Eq. 44) for trapped nanodust particles [33, 34]. For a particle released from a circular ecliptic orbit at 0.15 AU from the Sun $r_1 \sim 0.16$ AU and $r_2 \sim$

0.02 AU. Note that the perihelium is too close to the Sun for our solar wind model to be applicable: in any case, the nanodust grains would be destroyed by sublimation before reaching this point [33, 34].

(2) Nanodust particles created outside of the trapping region escape to large distances and acquire final velocities close to that of the solar wind. Figure (21) shows the particle velocity as a function of distance obtained for the sample of grains with different values of charge to mass ratio $q_d/\mathrm{m}= 10^{-4}$, 10^{-5}, 10^{-6} and 10^{-7} e/m$_p$ (corresponding to different grain size) starting from a circular orbit at the initial distance r=0.2 AU from the Sun. The grains with high q_d/m (10^{-5} e/m$_p$ and above) reach the velocity $\sim$300 km/s already at 1 AU.

The sharp "kinks" in the velocity profiles correspond to crossings of the heliospheric current sheet. Note that they occur only for the "focusing" magnetic field polarity (solid lines) when the particle drift direction is toward the sheet. Encounters with the current sheet reduce the final velocity.

The energy gain of the escaping particles is caused by the electric field $-\mathbf{V}\times\mathbf{B}$ which in our model is equal to $-\tilde{B}_r\Omega\bar{r}^2(sin\theta/r)\hat{\mathbf{e}}_\theta= \tilde{B}_r\Omega\bar{r}^2\nabla cos\theta$. In the absence of current sheet crossings, at which $\tilde{B}_r$, and therefore also the electric field changes sign, a change in the kinetic energy is unambigously associated with a change in $cos\theta$. Neglecting the radiative force, the conserved energy per mass is given by $v^2/2-GM_S/r+(q_d\tilde{B}_r/m)\Omega\bar{r}^2cos\theta$. Since the change in $cos\theta$ is at most ±2, the maximum possible change in the v^2-GM_S/r term is $\pm2\ (q_d/m)\tilde{B}_r\Omega\bar{r}^2$.

This provides a restriction on the energy gain by escaping particles [33] if their charge to mass ratio is too small. e.g. , for a particle with Q/m=10^{-6} e/m$_p$ ($(q_d/m)\tilde{B}_r\Omega\bar{r}^2$=(1.5 10^7 cm/s)^2) released from a Keplerian orbit at 0.2 AU, acceleration to 300 km/s is possible only if the change in $cos\theta$ reaches its maximum value, and impossible for smaller q_d/m (cf. Figure 21). As noted above, the argument works only if no current sheet crossings occur.

The acceleration of nanodust to high velocity can be simply understood for the case of small (Q/m=10^{-4} e/m$_p$ grains created beyond 1 AU, where the solar wind velocity is almost transverse relative to $\mathbf{B}$. In this case the initial Larmor radius is $\sim$0.1 of the distance r to the Sun and the particle motion can be viewed as a rotation around the magnetic field line carried at the solar wind speed. This results in the velocity oscillation with decreasing amplitude, since the adiabatic invariant is approximately conserved. For particles starting close to the Sun a simple picture of acceleration as well as trapping can be derived from the guiding centre approximation [33, 34].

The nanodust dynamics shows similarity to the pick-up process which occurs for the ions created by ionization of the neutral atoms that enter the solar wind from the interstellar medium or are emitted by planets or cometary sources. The resulting pick-up ions form a separate subpopulation of the solar wind plasma which differs from the bulk by the velocity distribution. The velocity distribution of the freshly picked-up ions has the form of a ring, but the pitch angle scattering transforms it into a shell distribution. The results presented in this section (which do not take into account pitch angle scattering for nanodust) can be compared to the study by Luhmann [137] of the heavy pick-up ions in the same scatter-free approximation.

(3) The influence of current sheet encounters on the dust trajectories needs to be fur-

ther studied. In the "focusing" configuration the drift of positively charged particles is directed towards the heliospheric current sheet. The probability of current sheet encounters increases for the larger nanodust grains ($Q/\mathrm{m}=10^{-5}$ rather than 10^{-4} $\mathrm{e/m}_p$) because of their larger Larmor radius and the drift magnitude.

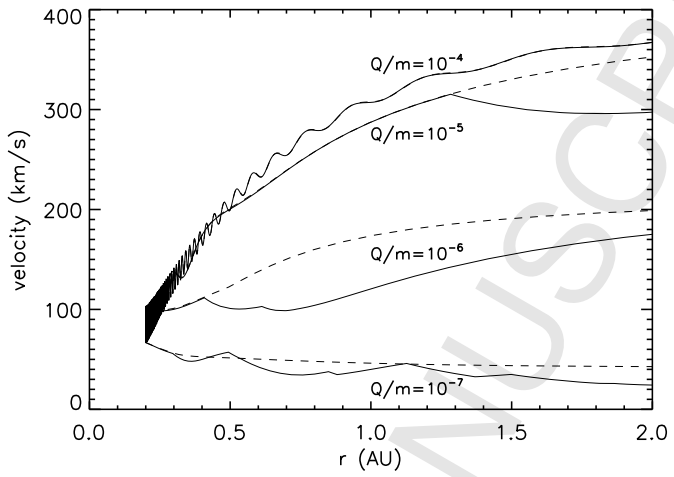

Figure 21: Velocity plotted against the distance from the Sun for the grains with $q_d/\mathrm{m}=10^{-4}$, 10^{-5}, 10^{-6}, and 10^{-7} $\mathrm{e/m}_p$ released from a circular orbit with the radius 0.2 AU near the ecliptic. Solid lines correspond to the focusing and dashed to defocusing magnetic field orientation.

On encountering the current sheet the particles commence drifting along its surface. The drift direction (for the focusing field) is opposite to the perpendicular component $\mathbf{V}_\perp$ of the solar wind velocity which explains why crossings of the current sheet reduce the final velocity of the escaping particles (Figure 21). Simulations show that, by drifting along the heliospheric current sheet, the nanodust particles can penetrate from the region near Jupiter to the vicinity of the Earth orbit [33].

5.5. Concluding remarks on dust dynamics

The study of dynamics of small charged dust grains reviewed in this section is is limited to the dynamics in the interplanetary medium, i.e. the solar wind, and does not address the dynamics in the magnetospheres of the giant planets that was recently studied based on the results of the Ulysses and Cassini space missions [89].

Some effects are also not addressed: The calculations reported above do not include the effects of time variations in the nanodust surface charge. Another important issue is the effect of solar wind fluctuations on the motion of charged dust grains. Similarly to high energy cosmic rays, the nanodust particles are characterized by high values of the rigidity $R \equiv pc/q_d$ where p=momentum. The grain with $q_d/\mathrm{m}=10^{-4}$ $\mathrm{e/m}_p$ moving at 300 km/s has $R = 10$ GV as does the proton with $\gamma = 1/\sqrt{(1 - v^2/c^2)} = 10$, and therefore the same values of R_L. The Larmor frequency $\mathrm{eB/m}_p\gamma$ of the ion is, however, much higher. In consequence, the nanodust grains and the high energy ions would preferentially couple to different frequencies of the solar wind fluctuations. The mean free path for pitch-angle scattering and the corresponding coefficients of diffusion for the nanodust particles cannot

be therefore simply obtained from the values for cosmic ray ions for the same rigidity. The effect on the dynamics of nanodust remains to be investigated.

In the vicinity of the Sun, the solar wind departs from the simplified model. The mechanism of trapping of the nanodust should therefore be re-examined taking into account the effects like plasma co-rotation as well as major variations in the flow and the field structure associated with the coronal mass ejections. The solar wind model needs to be improved also at larger distances by taking account of the interaction between slow and fast solar wind streams leading to the co-rotation interaction regions.

The deflection of nanodust in the magnetic field discussed in Section 5.3 for the case of dust at the outer edge of the heliosphere, depends not only on the strength of the magnetic field but also on the thickness of the region where the field acts. For example the Earth's magnetosphere, although the magnetic field there is stronger than near the heliospheric boundary, does not prevent the dust of nanometer size from reaching the Earth. For a nanodust grain with $q_d/m = 10^{-5}$ e/m$_p$ accelerated to 300 km/s by the solar magnetic field (see the discussion below in Section 5.4) the rigidity is 100 GV, far exceeding the geomagnetic cutoff ($\sim$ 15 GV at the Shuttle orbit near the Earth's equator).

6. Examples for ongoing research using space instrumentation

6.1. Nanodust in the solar wind

6.1.1. Nanodust observations in the solar system

The smallest dust particles, because of large surface-to-mass ratio can be expected to be most important for the dust interactions with surrounding particles and fields (Figure 22). The preceding Section (6.2) shows how the presence of the nanodust in the ionosphere can be inferred from the effects attributed to dust-plasma interactions and dusty plasma phenomena. The nanodust in space is, on the other hand, difficult to detect by astronomical observations: the data which suggest the presence of nanodust cannot be interpreted without ambiguity (Section 2.2.4). The in-situ measurements from spacecraft offer in this case a complementary approach. The instruments on ballistic atmospheric rockets observe nanodust with masses $\geq 3 \times 10^{-24}$kg, though at present these observations do not detect single particles and their interpretation rely on a number of different assumptions. Nanodust with masses of the order 10^{-21} kg, at that time also called attogram particles or very small dust grains (VSG), was already observed in-situ when the two Vega and the Giotto spacecraft crossed the path of comet Halley with high speed $\sim$70 - 80 km/s [224, 225]. During the past decade, fluxes of nanodust ejected from the magnetospheres of Jupiter and Saturn were quite intensively studied during several space missions and with different instruments and the reader is pointed to an overview presented by Hsu et al. [89]. The STEREO measurements described below suggest for the first time, that the nanodust is also widely distributed in interplanetary space and is a component of the solar system dust cloud.

6.1.2. Nanodust detection

The WAVES instrument on the twin Solar TErrestrial RElations Observatory (STEREO) spacecraft have observed a large number of voltage pulses interpreted as produced by nanodust impacting the spacecraft at a speed of several hundreds of kilometres per second

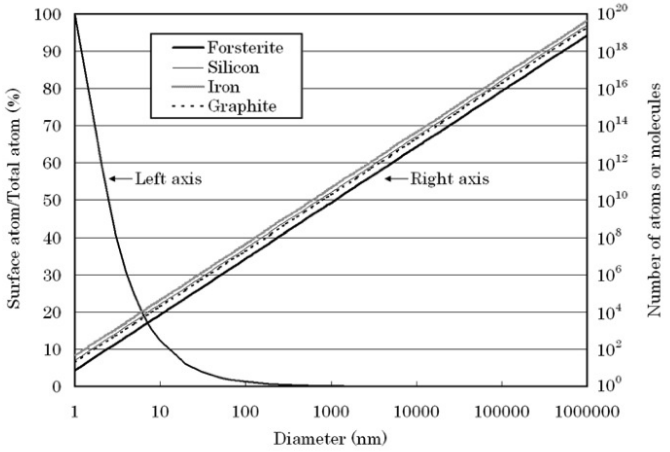

Figure 22: The particles relation between particle radius and the total number of atoms or molecules in a particles and the ratio of the total number of atoms or molecules to the number of those located on the surface. The materials are typical analogues for cosmic dust materials. Figure courtesy of Yuki Kimura, Sendai University, adapted from [106].

[168]. This serendipitous discovery came as a surprise since conventional dust detectors had not detected such interplanetary nanodust [66]. In retrospect, this detection might have been predicted since just before the first STEREO observations, Mann et al. [146] suggested that nanodust could be produced in the inner heliosphere and accelerated by the magnetized solar wind to nearly the solar wind speed. Motivated by the STEREO observations Czechowski and Mann subsequently studied the dynamics of nanodust in greater detail [33, 34]. The capability of wave instruments to measure dust was known since the 1980s, since the first in situ measurements of Saturn's dusty rings were performed by the radio [4] and the plasma wave [70] instruments on the spacecraft Voyager which did not carry conventional dust detectors.

Figure (23) shows how a wave instrument can detect high velocity dust impacts on a spacecraft, together with the properties of the ambient plasma [166].

The charge production upon dust impact was mentioned in Section (2.2.7). The collected charge Q_{impact} corresponding to the residual ionisation is a function of the grain mass and speed, which also depends on the material of both the grain and the target as well as on the impact angle; despite extensive theoretical calculations and simulations [110, 87], it remains largely empirical [115], with a typical relationship

$$\mathrm{Q}_{impact} \simeq m v^{3.5} \tag{53}$$

with Q_{impact} in Cb, m in kg, v in km s^{-1} [39, 155].

Applying Eq.(53) to fast nanodust (although the laboratory simulations do not reach this scale) shows that a 10 nm grain moving at 300 km/s in the solar wind, as predicted by dynamics [34], should produce the same impact charge as a grain $\sim$ 500 times more massive impacting at 50 km/s. Although laboratory simulations have not yet been performed with such fast nanodust, applying (53) to them appears adequate since the initial

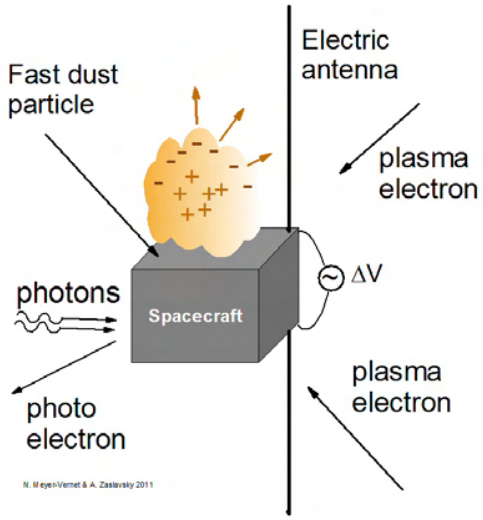

Figure 23: Principle of in situ measurements with an electric antenna onboard a spacecraft in a dusty plasma. Dust impacts at fast speed produce partial ionisation of the dust and target, yielding an expanding plasma cloud. This produces voltage pulses whose analysis reveals some dust properties. In addition, plasma particles passing-by the antennas (as well as impacting and ejected particles) produce a quasi-thermal electrostatic noise whose power spectrum reveals the plasma density, temperature and other properties. Figure adapted from [166].

identification of dust streams ejected by Jupiter by traditional detectors as 0.2 μm dust moving at about 50 km/s [63], based on a calibration varying as (53), was subsequently modified from dynamical arguments by multipliying the mass by 10^{-3} and the speed by about 7 [244]. Since $10^{-3} \simeq 7^{-3.5}$, this suggests that the $Q_{impact} \propto mv^{3.5}$ law still holds for nanodust.

Finally, it is noteworthy that a fast nanodust impact represents a huge incident power since for a grain of radius a and mass density ρ, the incident kinetic energy $\rho(4\pi a^3/3)v^2/2$ comes over the surface $\sim \pi a^2$ during a time $\sim a/v$, which yields a power $P \sim \rho v^3$. For $\rho \sim 2.5 \times 10^3$ kg m^{-3} and $v \sim 300$ km/s, this yields $P \sim 10^{20}$ W/m^2 - a huge power, greater by several orders of magnitude than that involved in laboratory simulations [166].

6.1.3. Nanodust as a component of the solar system dust cloud

The flux of nanodust derived from the STEREO measurements is close to the curve obtained from extrapolating the previous observations near 1 AU to smaller sizes as seen in Figure (24), which shows the average fluxes of nanodust derived from the plasma wave measurements [168, 166, 13, 243]. It was mentioned above that the collisional evolution of the dust cloud generates dust over a broad range of sizes described in models of a flux versus mass curve at 1 AU [62, 25, 94]. Its extrapolation to nanometric sizes is shown in Figure (24) and the indicated flux curve $\sim m^{-5/6}$ results from the small bodies fragmentation theory [40] and would be observed in the absence of other effects. Note, that the same instrument also observed the impacts of larger dust particle, including impacts that could be attributed to interstellar dust [13, 243].

The shape of the curve suggests that the nanodust is formed in the same way as

the larger dust particles, i.e. by collisional fragmentation, even though this might be taken with caution, because of the large error bars of the measurements. In addition, the nanodust flux is highly time-variable, which is not observed for the larger dust. The dust dynamics outlined above (Section 5.4) suggests that a fraction of the nanodust that forms in the inner solar system is ejected outward and crosses Earth orbit with large speed so that it can cause the observed STEREO events.

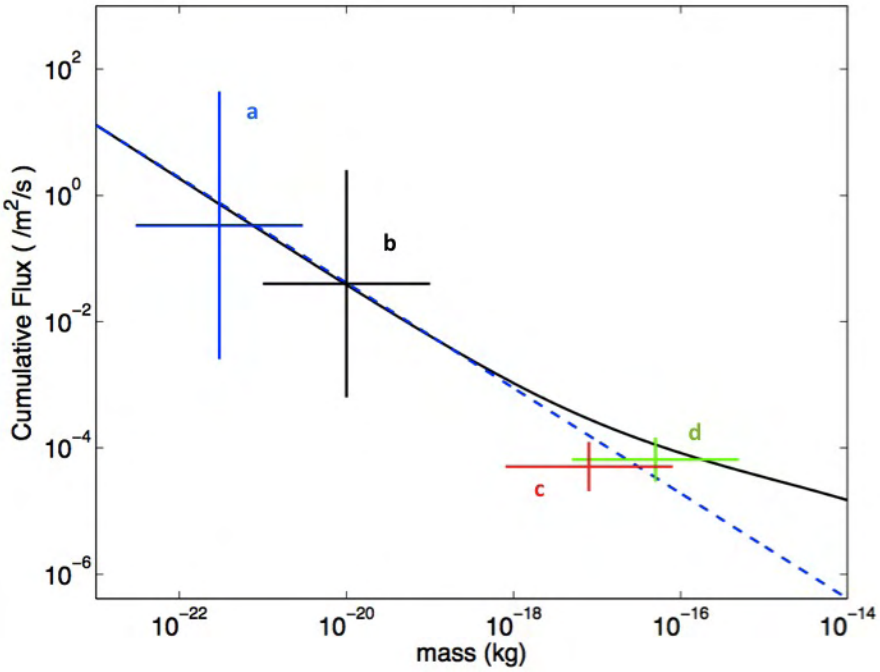

Figure 24: The models of cumulative flux of dust particles of mass greater than m and flux estimates derived from Stereo observations ([168, 243], further discussed in Section 6.1.2). The solid line is extrapolated from observational interplanetary dust flux models [62, 25], the dashed line denotes the collisional flux $\sim m^{-5/6}$ [40] in the absence of other processes that limit the lifetime of the dust. The observational data from STEREO are (a) the 3 - 12 nm average flux derived from 4 years of measurements, (b) the average flux derived from the first two years of measurements, (c) the derived flux of larger dust ($\sim$ 0.1μm), and (d) the flux of $\sim$ 0.1 - 0.3 μm interstellar dust. Figure adapted from [243].

In order to estimate the flux of nanodust at Earth orbit, Czechowski and Mann [33] estimated the production rate of the nanodust grains by dust-dust collisions inside 1 AU within a circum-solar disk and calculated their trajectories. The calculations show high speeds for the 3 to 10 nm grains (i.e. q_d/m=10^{-5}-10^{-4} e/m_p, see Section 5). Their average radial component $< v_r >\sim$240-280 km/s is about twice the azimuthal component $< v_\phi >\sim$100-140 km/s, while $< v_\theta >$ is much smaller but with a large spread. Of all grains in this size range created in the disk, only a fraction of $\sim$0.1-0.2 was found to escape to 1 AU; the remaining ones were trapped. The fraction of the grains escaping passing 1 AU close to the ecliptic (within $\pm 13^o$ ecliptic latitude) was found to be 0.3-0.45 for defocusing and close to 1 for the focusing field polarity, the magnetic field structure is described above (Section 5.1).

The fact that most of the produced nanodust falls into the trapped region suggests a

possible explanation [33] for the observed large time variations of the nanodust [168]. A small change in the boundary of the trapping region, caused by a temporal change in the solar wind parameters, is likely to produce a large change in the flux at 1 AU, although other dynamical effects, the variation of the detection efficiency and/or the variation of the dust production may also play a role. A recent study of the trajectories shows that even for a constant production rate near the Sun the interaction with the interplanetary magnetic fields can generate an intermittent flux of the nanodust at the STEREO spacecraft [102].

An interesting point for future studies, which is also relevant for the dust evolution in the interstellar medium, is to verify that the empirical laws describing collision fragments of larger size are valid down to nanometer sizes and to determine by observations the smallest size of the collision fragments [144]. The collision velocities in the interstellar medium and near the Sun are similar and the rates of dust production important for understanding the physics of the interstellar medium. The dust formation process is also important for the processes in the Earth ionosphere, though it follows a different path there.

6.2. Cosmic dust in the Earth atmosphere: plasma interactions

6.2.1. Deposition of meteoroid material and its observations

Many different estimates exist of the total amount of meteoroid matter that falls onto Earth. For an evaluation of these different observations and for a discussion of the resulting chemical phenomena see [190]. According to the model by Ceplecha et al., which covers a broad size interval as well as observations over up to 100 years, the flux amounts to an average 10 tons/day and at times locally more [25]. From this model an average mass flux $4.2 \cdot 10^6$ kg yr^{-1} is found for meteoroids with masses $<10^{-2}$ kg. This is the mass range of objects that produce meteor phenomena during which a large fraction of meteoroid matter is delivered into the atmosphere. The rate of this deposition of meteoric material into the atmosphere steeply peaks at 90 to 80 km altitude [88].

Figure 25: A noctilucent cloud, NLC observed during the night 26-27 June 2005 from Moscow. Photograph courtesy of Peter Dalin, The Swedish Institute of Space Physics, IRF, Kiruna, Sweden.

The atmosphere at this altitude consists of neutral atmospheric constituents N_2, O_2, O and ions, mainly O^+, NO^+, $O_2{}^+$. The ion amount varies e.g. with geomagnetic activity,

solar cycle, season and time of day, and with latitude. The most common metallic ions from the vaporized meteoroid material are Fe^+, Mg^+ and Si^+. They sometimes lead to strong narrow ionization layers at this altitude, sporadic E layers. Layers of metallic neutrals are also observed. Part of the meteoric material stays solid or re-condenses from the vapor to nanometer-sized particles, known as meteoric smoke. Depending on temperature and water vapor pressure, water ice condenses on the smoke and forms larger particles [103, 196]. The ice particles are observed in two phenomena at altitudes 80-95 km: noctilucent clouds (NLC) and Polar Mesosphere Summer Echoes (PMSE) (e.g. [48]). NLCs, also known as Polar Mesospheric Clouds, are optical phenomena (Figure 25) that are caused by Mie-scattering of ice particles of size above the nanometric range (e.g. [10]). PMSE, in contrast, are most likely produced in the presence of ice grains, possibly (at least in part) of sub-visible nanometric sizes (e.g. [196, 77]). They are strong backscatter signals of radio waves, observed since 1980s during summer at polar latitudes, less frequently at lower latitude. Initially these were detected around 50 MHz, but now are observed in a broad range of 50 - 1000 MHZ and occasionally beyond.

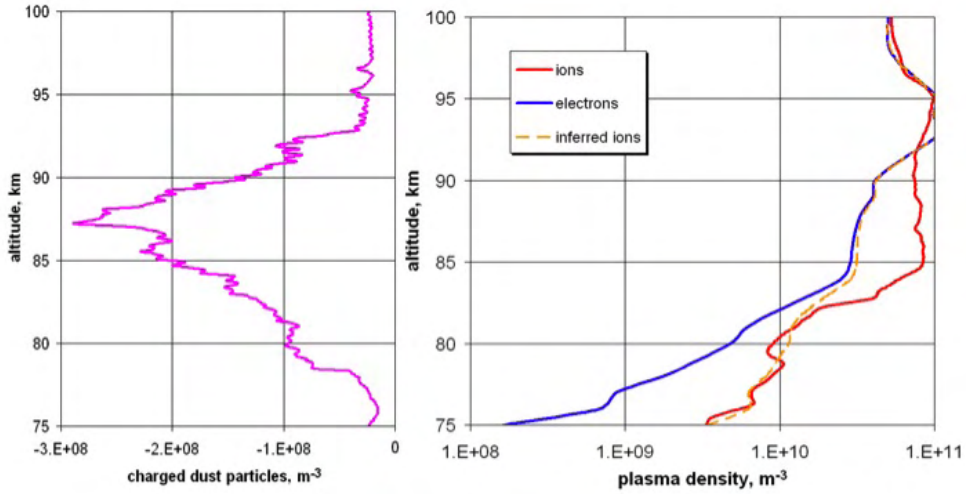

Figure 26: Negatively charged nanodust measured on a sounding rocket ECONOMA flight. Electron and ion densities measured in the same flight (right panel). The charged dust particles are of the mass range 500 to 2000 amu. Figure courtesy of Martin Friedrich, from [49] reproduced with permission of the authors.

6.2.2. Dust charging and PMSE

The PMSE are thought to be caused by spatial variation of the refractive index, due to variation in electron density. The changes of electron density appear in presence of charged dust particles. Since the dust particles have high content of water ice they are

diminished in size when temperature rises above the water ice melting temperature and this could explain the seasonal variation: the mesosphere is coldest in summer. The broad scenario [196] is that gravity waves in the neutral atmosphere propagate upwards and generate eddies at PMSE altitude. The charged dust particles are carried with the neutrals, and due to their charge, influence electron distribution and generate electron density variations. With index of refraction at the (angular) frequency ω, $\epsilon^{1/2} = 1 - \omega^2/\omega_p^2$ and $\omega_p \sim (n_e e^2/\epsilon_0 m_e)^{1/2}$, its variation directly results from structures in the electron density distribution.

We have seen in Section 4.2 that when photoelectron emission is negligible, which is the case for pure ice at mesospheric altitudes, dust grains tend to be negatively charged. Furthermore, at $\simeq 150$ K, the Landau radius $r_L \simeq 0.1$ μm, so that Eq.(35) shows that the vast majority of nanograins should carry one electron charge. Hence, nanograins act as a sink for electrons and change the plasma number densities to achieve quasi-neutrality (Section 4.7). The dust can therefore drive plasma electron structures.

This physical process seems to be the key to solve the theoretical problem posed by observation of PMSE (e.g. [195] and references therein). Indeed, such observations of coherent scatter require structures in the refractive index (determined by the electron number density) at the Bragg scale, i.e. at half the radar wavelength. But the VHF wavelength $\simeq 3$ m is much smaller than the inner scale of turbulence of the neutral gas, so that the irregularities should be quickly dissipated by molecular diffusion. Anyway, PMSE are often observed without simultaneous neutral air turbulence at the same altitude. So, the solution is not as simple as seems from first sight.

This long-standing problem has been solved by calculating the diffusivity of electrons in the complex dusty plasma of the mesosphere. The presence of dust reduces the electron diffusivity, so that they decouple from neutrals at small scales. On the other hand, turbulent velocities of neutrals transport ice particles, which because of their charging produce small electron density structures of long life-time (due to the small diffusivity), that can therefore exist long after air turbulence has ceased [196]. These electron density structures are responsible of the observed radio wave scattering via the changes in refractive index.

Even though these processes are now qualitatively rather well understood [48] and have been measured (Figure 26), the creation of the dust particles which originate them still poses several problems, which may also be solved by considering the effect of the dust charging on the grain formation [103, 69, 157]. Indeed, the smoke particles that form from the material produced from ablation of meteoroids entering the Earth's upper atmosphere are efficient as nucleation sites for the formation of ice particles because of their electric charge, which lowers considerably the energy barrier against nucleation [69].

6.2.3. Experiments to study the dusty plasma in the atmosphere

An observation to better understand the PMSE is to study the variation of the radar echo with scattering angle. Figure (27) shows the first bi-static observation of a PMSE above the EISCAT site in Tromsø, Norway on 11 July 2011 around noon. The local time is + 1 hour from UTC given in the figure. The radio signal was transmitted from the Tromsø - EISCAT VHF antenna. The back scattered signal was received in Tromsø with the same antenna and in Kiruna, Sweden. Tromsø measurements are shown in the upper panel in units of electron density (equivalent density in the PMSE layer), the Kiruna measurements

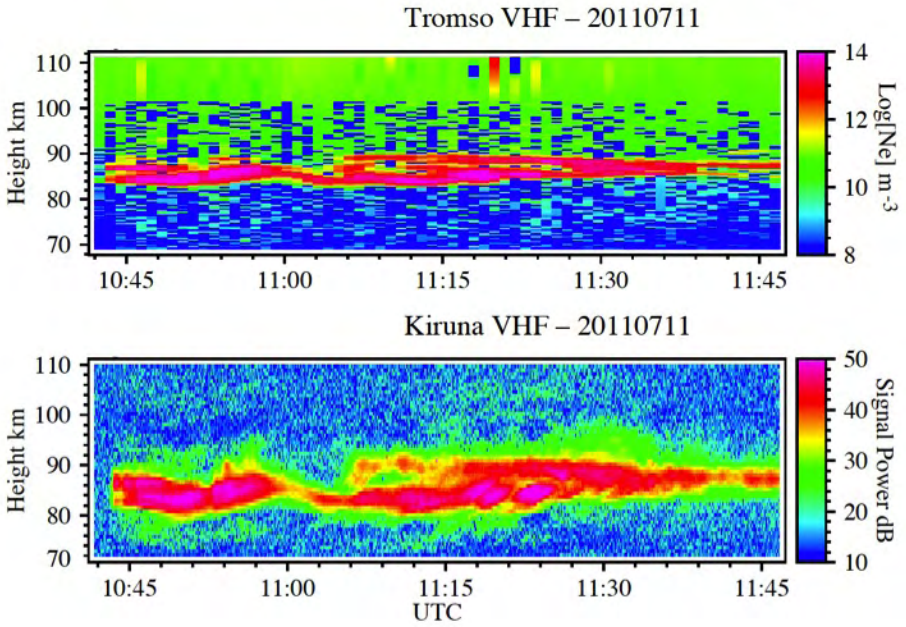

Figure 27: First bi-static observation of polar mesospheric summer echoes (PMSE) generated by plasma irregularities in the presence of charged dust on 11 July 2011. The radar signal was transmitted with the EISCAT VHF antenna near Tromsø (69°35' N, 19°14'E). The upper panel shows the backscattered signal received from EISCAT VHF and the lower panel the signal received from the EISCAT_3D test array in Kiruna (67°52' N, 20°26'E). Figure courtesy of Cesar La Hoz, University of Tromsø, Norway.

are shown in the lower panel in arbitrary units of signal power. The time resolutions of the measurements are 1 minute and 4.8 seconds, the height resolutions 0.4 km and 0.7 km for Tromsø and Kiruna observations, respectively. These observations prove the occurrence of the radar echoes at different aspect angles, which possibly provides a clue towards understanding the scattering process. The baseline distance between the Tromsø and Kiruna antennae is 234 km, so this PMSE was observed at quite large scattering angle of 69 degree. The dependence of the signal on aspect angle is important for a closer study of the reflection process and also for comparing the radar reflectivities that are measured with different instruments [216]. The Kiruna measurements were made with a test array for the planned EISCAT3D instrument [228], a multi–static phased–array radar system, that, among other things, would provide the opportunity to study the spatial structure of PMSE in more detail.

A topic that we do not want to elaborate here because of its complexity is the response of PMSE signals to Heating experiments. During these experiments the absorption of radio waves of several MHz locally changes the electron temperature in the ionosphere [207, 129]. For instance Mahmoudian and Scale [138] estimate that the electron temperature increases by factor 3. Chilson et al. [27] discovered that during heating the PMSE echoes are weakened. This possibly happens because the enhanced electron temperature improves diffusion and density fluctuations are smoothed out more quickly, though Belova et al. studied the response time and based on that come to the conclusion that this is not

the only effect that plays a role [14].

While these atmospheric phenomena are interesting topics for studying complex dusty plasmas, they are also important for understanding the physics of the atmosphere including possibly the human impact onto the atmosphere, possibly resulting in an increased abundance of water vapor and a decreased mesospheric temperature during summer [220, 54, 196, 190]). The presence of the ice-particles, in turn, influences the chemical processes in the atmosphere. The records reporting the observations of NLC for decades (see eg. [35]) show that their number possibly increases over the years. The analysis is however difficult because of a number of effects that influence the observations. The effects include the change of observation methods with time as was for instance shown with a detailed analysis of 43 year of NLC observations from the UK and Denmark [111].

Finally similar echoes are observed during winter at lower altitude, i.e. Polar Mesospheric Winter Echoes, PMWE. The PMWE are observed less frequently, they are weaker than PMSE and not correlated with NLC. It is assumed that they are less frequently observed, because at lower altitude the electron densities are smaller and not sufficient to produce the radar echo. They are possibly occurring during enhanced ionization, for instance, due to i.e. solar proton events or geomagnetic activity and most likely will be observed more frequently during the recent winters close to solar maximum, since electron densities are then higher in the lower atmosphere (see e.g. [215]). Their studies may help to distinguish the role of dust and of other factors in the formation of the radar echoes.

7. Acknowledgement

The authors acknowledge helpful discussions with Ingemar Häggström, Aigen Li, and Arnaud Zaslavski, the support of Ronald Redmer as the scientific editor, and the comments of an anonymous reviewer, as well as the help of colleagues whose figures were reproduced in this article. IM was supported through a guest professorship at the Physics Department, Umeå University.

References

[1] M. M. Abbas, D. Tankosic, P. D. Craven, et al., Astrophys. J. 645 (2006) 324-336.

[2] M. M. Abbas, D. Tankosic, A. C. LeClair, J. F. Spann, Astrophys. J. 756 (2006) 1-14.

[3] L. J. Allamandola, A.G.G.M Tielens, J.R. Barker, Astrophys. J. 290 (1985) L25-L28.

[4] M. Aubier, N. Meyer-Vernet, B.M. Pedersen, Geophys. Res. Lett. 10 (1983) 5.

[5] S. Auer, in: Grün, E. et al. (Eds.), Interplanetary dust, Springer Heidelberg, 2001 pp. 385-439.

[6] S. Auer, S. Kempf, E. Grün, in: H. Krüger, A. Graps (Eds.), Workshop on Dust in Planetary Systems, ESA SP-643, 2007, p. 177.

[7] E.L.O. Bakes, A.G.G.M. Tielens, Astrophys. J. 427 (1994) 822.

[8] A. Balogh, R. J. Forsyth, in: E. R. Priest, F. Moreno-Insertis, R. A. Harris (Eds.), Crossroads for European Solar and Heliospheric Physics. Recent Achievements and Future Mission Possibilities, ESA SP-417, 1998, pp.45-54.

[9] A. Balogh, in: B. Montesinos, A. Gimenez, E. F. Guinan (Eds.), The Evolving Sun and its influence on Planetary Environments, ASP Conf. Series 269, San Francisco, Astronomical Society of the pacific, 2002, pp.37-71.

[10] G. Baumgarten et al., J. Geophys. Res. 113 (2008) D06203.

[11] A. Beck, N. Meyer-Vernet, Am. J. Phys. 76 (2008) 934-936.

[12] C. A. Beichman, Annu. Rev. Astron. Astrophys. 25 (1987) 521-563.

[13] S. Belheouane, A. Zaslavsky, N. Meyer-Vernet, et al. Solar Phys. 281 (2012) 501–506.

[14] E. Belova, P. B. Chilson, S. Kirkwood, M. T. Rietveld, J. Geophys. Res. 108 (2003) CiteID 8446.

[15] M. Beránek, I. Richterová, Z. Němeček, J. Pavl, J. Šafránková, European Physical Journal D 54 (2009) 299-304.

[16] L. Biermann, Mém. Soc. Roy. Sci. Liège (Ser. 4) 13 (1953) 291.

[17] D. A. Biesecker, P. Lamy, O. C. St. Cyr, Icarus 157 (2002) 323-348.

[18] M. Booth, M.C. Wyatt, A. Morbidelli, et al. Mon. Not. Roy. Astron. Soc. 399 (2009) 385-398.

[19] J.A. Burns, P.L. Lamy, S. Soter, Icarus 40 (1979) 1-48.

[20] J. A. Burns, D. P. Hamilton, M. R. Showalter, in: E. Grün, B. A. S. Gustafson, S. F. Dermott, H. Fechtig (Eds.), Interplanetary Dust, Springer, Heidelberg, 2001, pp. 641-725.

[21] Bradley, J., and 12 colleagues, Science 307 (2005) 244-247.

[22] D.E. Brownlee, D.J. Joswiak, S.G. Love, A. O. Nier, D. J Schlutter, J. P. Bradley, Lunar Plan. Sci. 24 (1993) 205-206.

[23] H. Bruining, Physics and Applications of Secondary Electron Emission, Pergamon, New York, 1954.

[24] V. Carbone, Space Sci. Rev. (2012), DOI 10.1007/s11214-012-9907-z.

[25] Z. Ceplecha, J. Borovička, W.G. Elford, et al., Space Sci. Rev. 84 (1998) 327-471.

[26] J. W. Chamberlain, D. M. Hunten, Theory of Planetary Atmospheres: An Introduction to their Physics and Chemistry, Academic press, London, 1987.

[27] P. B. Chilson, E. Belova, M. T. Rietveld, S. Kirkwood, U.-P. Hoppe, Geophys. Res. Lett. 27 (2000) 3801-3804.

[28] V. W. Chow, D. A. Mendis, M. Rosenberg, J. Geophys. Res. 98 (1993) 19,065-19,076.

[29] D.D. Clayton, L.R. Nittler, Annu. Rev. Astron. Astrophys. 42 (2004) 39Ð78.

[30] M. Compiegne, N. Flagey, A. Noriega-Crespo, P.G. Martin, J.P. Bernard, R. Paladini, S. Molinari, Astrophys. J. Lett.724 (2013) L44-L47.

[31] A. Czechowski, I. Mann, J. Geophys. Res. 108 (2003) A10 13-1.

[32] A. Czechowski, I. Mann, Astron. Astrophys. 410 (2003) 165.

[33] A. Czechowski, I. Mann, Astrophys. J. 714 (2010) 89-99 (Errata: ApJ 732 (2011) 127, ApJ 740 (2011) 50).

[34] A. Czechowski, I. Mann, in: I. Mann, N. Meyer-Vernet, A. Czechowski (Eds.), Nanodust in the solar system: discoveries and interpretations, Springer Heidelberg, 2012, pp.47-75

[35] P. Dalin, History of Geo- and Space Sciences 3 (2012) 87-97.

[36] P. Démoulin, 2010, in: M. Maksimovic, K. Issautier, N. Meyer-Vernet, M. Moncuquet, F. Pantellini (Eds.), 12th International Solar Wind Conference, AIP CP1216, American Institute of Physics, 2010, pp. 329-334.

[37] S.F. Dermott, K. Grogan, D.D. Durda, S. Jayaraman, T.J.J. Kehoe, S. Kortenkamp, M. C. Wyatt, in: E. Grün, B. A. S. Gustafson, S. F. Dermott, H. Fechtig (Eds.), Interplanetary Dust, Springer Heidelberg, 2001, pp. 569-639.

[38] S.F. Dermott, D.D. Durda, K. Grogan, T. J.J. Kehoe, in: W. F. Bottke, Jr., A. Cellino, P. Paolicchi, R. P. Binzel (Eds.) Asteroids III, The University of Arizona Press, Tuscon, 2002, pp. 423-442.

[39] H. Dietzel et al., J. Phys. E. Scientif. Instr. 6 (1973) 209.

[40] J.S. Dohnanyi, J. Geophys. Res. 74 (1969) 2531Ð2554.

[41] S. Drapatz, K.W. Michel, Z. Naturforsh. 29a (1974) 870.

[42] B. T. Draine, Astrophys. J. Sup. Ser. 36 (1978) 595-619.

[43] B. T. Draine, Annu. Rev. Astron. Astrophys. 41 (2003) 241-289.

[44] B. T. Draine, E. E. Salpeter, Astrophys. J. 231 (1979) 77-947.

[45] B. T. Draine, B. Sutin, Astrophys. J. 320 (1987) 803-817.

[46] H. Fechtig, C. Leinert, O. Berg, in: E. Grün, B. A. S. Gustafson, S. F. Dermott, H. Fechtig (Eds.), Interplanetary Dust, Springer Heidelberg, 2001, pp. 1-55.

[47] B. Feuerbacher, B. Fitton, J. Appl. Phys. 43 (1972) 1563.

[48] M. Friedrich, M. Rapp, Surv. Geophys. 30 (2009) 525-559.

[49] M. Friedrich and 7 co-authors, Annales Geophysicae 30 (2012) 1495-1501.

[50] P. C. Frisch and 15 colleagues Astrophys. J. 525 (1999) 492-516.

[51] P.C. Frisch, M. Bzowski, E. Grün, et al., Space Sci. Rev. 146 (2009) 235-273.

[52] H. B. Garrett, Rev. Geophys. Space Phys. 19 (1981) 577-616.

[53] H. B. Garrett, A. R. Hoffman, IEEE Trans. Plasma Sci. 28 (2000) 2048-2057.

[54] M. Gadsden, J. Atmos. Solar Terr. Phys. 52 (1990) 247-251.

[55] R. H. Giese, B. Kneissel, U. Rittich, 68 (1986) 395.

[56] C. K. Goertz, W. H. Ip, Geophys. Res. Lett. 11 (1984) 349.

[57] C. K. Goertz, Rev. Geophysics 27 (1989) 271-292.

[58] R. Gomer, Field Emission and Field Ionisation, Harvard Univ. Press, Cambridge, Mass., 1961.

[59] N.N. Gorkavyi, L.M. Ozernoy, T. Taidakova, T., J. C. Mather, in: E. P. Smith, K. S. Long (Eds.) ASP Conference Series 207 (2000) 462 Ð 467.

[60] R. J. L. Grard, J. Geophys. Res. 78 (1973) 2885-2906.

[61] K. Grogan, S.F Dermott, D. D. Durda, Icarus 152 (2001) 251-267.

[62] E. Grün H.A. Zook, H. Fechtig, R. H. Giese, R.H., Icarus 62 (1985) 244.

[63] E. Grün et al., Science 257(1992) 1550.

[64] E. Grün, B. Gustafson, I. Mann, et al., Astron. Astrophys. 286 (1994) 915-924.

[65] E. Grün, H. Krüger, M. Landgraf, 2000, in: A. Fitzsimmons, D. Jewitt, R.M. West (Eds.), Minor bodies in the outer solar system, ESO Workshop, Springer, Heidelberg, 2000, pp. 99-108.

[66] E. Grün et al., in: E. Grün et al. (Eds.), Interplanetary dust, Springer Heidelberg, 2001, pp. 295-323.

[67] E. Grün, M. Horanyi, Z. Sternovsky Planet. Space Sci. 59 (2011) 1672-1680.

[68] J. Gumbel, J. Geophys. Res. 106 (2001) 10553-10564.

[69] J. Gumbel, L. Megner, J. Atmos. Solar Terr. Phys. 71 (2009) 1225-1235.

[70] D.A. Gurnett, E. Grün, D. Gallagher, W.S. Kurth, F.L. Scarf, Icarus 53 (1983) 236-254.

[71] D.A. Gurnett, J.A. Ansher, W.S. Kurth, J.L. Granroth, Geophys. Res. Lett. 24 (1997) 3125.

[72] D.P. Hamilton, E. Grün, M. Baguhl, 1996, in: B.A.S. Gustafson and M.S. Hanner (Eds.), Physics, chemistry and dynamics of interplanetary dust, ASP Conf. Ser. 104, IAU Colloq. 150, (1996) p. 31-34.

[73] M. S. Hanner, Space Sci. Rev. 90 (1999) 99 - 108.

[74] M. S. Hanner, R. H. Giese, K. Weiss, R. Zerull, Astron. Astrophys. 104 (1981) 42-46.

[75] M. S. Hanner, M. E. Zolensky, in: T. Henning (Ed.), Astromineralogie, Springer Berlin, 2010, pp. 203-232.

[76] D. E. Harker, C. E. Woodward, D. H. Wooden, R. S. Fisher, C. A. Trujillo, Icarus, 191 (2007) 432.

[77] T. Hartquist, O. Havnes, M. Kassa, Astron. Geophys, 50 (2009) 1.08-1.14.

[78] M. G. Hauser, F. C. Gillett, F. J. Low, et al. Astrophys. J. 278 (1984) L15-L18.

[79] O. Havnes, O., L. I. Næsheim, Annales Geophysicae 25 (2007) 623-637.

[80] O. Havnes, G. E. Morfill, C. K. Goertz, J. Geophys. Res. 89 (1984) 10,999.

[81] O. Havnes, J. Trøim, T. Blix, et al., J. Geophys. Res. 101(1996) 10839-10848.

[82] J. K. Hillier, S. F. Green, N. McBride, et al. Icarus 190 (2007) 643-654.

[83] T. Hoang, B. T. Draine, A. Lazarian, Astrophys. J. 715 (2010) 1462-1485.

[84] T.E. Holzer, Annu. Rev. Astron. Astrophys. 27 (1989) 199-234.

[85] W. Honda M., et al., Astrophys. J. 601 (2004) 577.

[86] P. Hoppe, in: Landolt-Boernstein New Series VI/4B 4_30, Springer, Berlin.

[87] K. Hornung, J. Kissel, Astron. Astrophys. 291 (1994) 1.

[88] D.M. Hunten, R.P. Turco, O.B. Toon, J. Atm. Sci. 37 (1980) 1342-1357.

[89] S. Hsu, H. Krüger, F. Postberg, in: I. Mann, N. Meyer-Vernet, A. Czechowski (Eds.), Nanodust in the solar system: discoveries and interpretations, Springer, Heidelberg, 2012, pp. 77-117.

[90] S. I. Ipatov, A. S. Kutyrev, G. J. Madsen, J. C. Mather, S. H. Moseley, R. J. Reynolds, Icarus 194 (2008) 769-788.

[91] M. Ishiguro, M. Ueno, in: I. Mann, A. M. Nakamura, T. Mukai (Eds.), Small Bodies in Planetary Systems, Springer. Berlin, Heidelberg, 2009, pp. 231-252.

[92] M. Ishiguro, R. Nakamura, Y. Fujii, T. Mukai, Publ. Astron. Soc. Japan 51 (1999) 363-366.

[93] M. Ishiguro, R. Nakamura, Y. Fujii, et al. Astrophys. J. 511 (1999) 432-435.

[94] H. Ishimoto, Astron. Astrophys. 362 (2000) 1158.

[95] J. D. Jackson, Classical electrodynamics, 3rd Ed., Wiley, 1999, p. 61.

[96] J. H. Jeans, The Dynamical Theory of Gases, Dover, New-York, 1954.

[97] E. J. Jensen, G. E. Thomas, J. Geophys. Res. 86 (1991) 18,603-18,615.

[98] D. Jewitt, Earth, Moon, and Planets 72 (1996) 185-201.

[99] D. Jewitt, J. Lee, Astron. J. 140 (2010) 1519-1527.

[100] T. D. Jones, L. A Lebofsky, J. S. Lewis, M. S. Marley, Icarus 88 (1990) 172.

[101] J. H. Jonker, Philips Res. Rep. 7 (1952) 1.

[102] A. Juhasz, M. Horanyi, Geophys. Res. Lett. 40 (2013) 2500 - 2504.

[103] O. Kalashnikova, M. Horányi, G. E. Thomas, O. B. Toon, Geophys. Res. Lett. 27 (2000) 3293-3296.

[104] Kelsall, T. et al. Astrophys. J. 508 (1998) 44-73.

[105] S. Kempf, U. Beckmann, R. Srama, M. Horanyi, S. Auer, E. Grün, Planet. Space Sci. 54 (2006) 999-1006.

[106] Y. Kimura, in: I. Mann, N. Meyer-Vernet, A. Czechowski (Eds.), Nanodust in the solar system: discoveries and interpretations, Springer, Heidelberg, 2012, pp. 31-46.

[107] H. Kimura, I. Mann, Astrophys. J. 499 (1998) 454-462.

[108] H. Kimura, L. Kolokolova, I. Mann, Astron. Astrophys. 407 (2003) L5-L8.

[109] H. Kimura, I. Mann, E. K. Jessberger, Astrophys. J. 582 (2003) 846-858.

[110] J. Kissel, F.R. Krüger, Appl. Phys. A 42 (1987) 69.

[111] S. Kirkwood, P. Dalin, A. Rechou, Ann. Geophys. 26 (2008) 1243-1254.

[112] Knight, M. M., A'Hearn, M. F., Biesecker, et al., Astron. J. 139 (2010) 926-949.

[113] L. Kolokolova, M. S. Hanner, A.-C. Levasseur-Regourd, B. Å. S.Gustafson in: Comets II, University of Arizona Press, 2004, pp. 577-604.

[114] A. Krivov, H. Kimura, I. Mann, Icarus 134 (1998) 311-327.

[115] F. R. Krüger, Adv. Space Res. 17 (1996) 1271.

[116] H. Krüger, N. Altobelli, B. Anweiler, et al. Planet. Space Sci. 54 (2006) 932-956.

[117] H. Krüger, H., E. Grün, Space Sci. Rev. 143 (2009) 347-357.

[118] W. S. Kurth, T.F. Averkamp, D.A. Gurnett, Z. Wang, Planet. Space Sci. 54 (2006) 988-998.

[119] J.G. Laframboise and L.W. Parker, Phys. Fluids 16 (1973) 629-636.

[120] R. Lallement, P. Bertin, R. Ferlet, A. Vidal-Madjar, J. L. Bertaux, Astron. Astrophys. 286 (1994) 898-908.

[121] M. Landgraf, J. Geophys. Res. 105 (2000) 10303.

[122] M. Landgraf, H. Krüger, N. Altobelli, E. Grün, J. Geophys. Res. 108 (2003).

[123] G. Le Chat, K. Issautier, N. Meyer-Vernet, Solar Phys. 279 (2012) 197.

[124] G. Le Chat et al. Solar Phys. , 286 (2013) 349-559.

[125] C. Leinert, S. Bowyer, L.K. Haikala, et al. Astron. Astrophys. Suppl. 127 (1998) 1-99.

[126] Levasseur-Regourd, A.C., Mann, I., Dumont, R. & Hanner, M.S, in: E. Grün, B.A.S. Gustafson, S.F. Dermott & H. Fechtig (Eds.), Interplanetary Dust, Springer, Heidelberg, 2001, pp. 57-82.

[127] Lemaire, J., 2010, in: M. Maksimovic, K. Issautier, N. Meyer-Vernet, M. Moncuquet, F. Pantellini (Eds.), 12th International Solar Wind Conference, AIP CP1216, American Institute of Physics, 2010, pp. 3-7.

[128] E.H. Levy, J.R. Jokipii, Nature 264 (1976) 423-424.

[129] T. B. Leyser, A. Y.Wong, Reviews of Geophysics 47 (2009) 1001.

[130] A. Li, Astrophysics of Dust, 309 (2004) 417.

[131] A. Li, J. Phys. Conf. Ser. 6 (2005) 229Ð48.

[132] A. Li, Astrophys. J. 622 (2005) 965Ð969.

[133] A. Li, I. Mann, in: I. Mann, N. Meyer-Vernet, A. Czechowski (Eds.), Nanodust in the solar system: discoveries and interpretations, Springer, Heidelberg, 2012, pp. 5-30.

[134] T.J. Linde, T.I. Gombosi, J. Geophys. Res. 105 (2000) 10411.

[135] J.-C. Liou, S.F. Dermott, Y.L. Xu, Y. L., Planet. Space Sci. 43 (1995) 717-722.

[136] C. M. Lisse, K. E.Kraemer, J. A. Nuth, A. Li, D. Joswiak, Icar, 187 (2007) 69

[137] J.G. Luhmann, 2003, Astrophys. J. 592 (2003) 1241-1251.

[138] A. Mahmoudian, W. A. Scales, Geophys. Res. Lett. 117 (2012) 6221.

[139] I. Mann, Astron. Astrophys. 261 (1992) 329-335.

[140] I. Mann, in: Landolt Boernstein New Series VI/4B 4_29, Springer, Berlin.

[141] I. Mann, Annu. Rev. Astron. Astrophys. 48 (2010) 173.

[142] I. Mann, H. Kimura, J. Geophys. Res. 105 (2000) 10317-10328.

[143] I. Mann, A. Czechowski, Astrophys. J. 621 (2005) L73-L76.

[144] I. Mann A. Czechowski, in: I. Mann, N. Meyer-Vernet, A. Czechowski (Eds.), Nanodust in the solar system: discoveries and interpretations, Springer, Heidelberg, 2012, pp. 195-219.

[145] I. Mann, N. Meyer-Vernet, A. Czechowski, in: M. Maksimovic, K. Issautier, N. Meyer-Vernet, M. Moncuquet, F. Pantellini (Eds.), 12th International Solar Wind Conference, AIP CP1216, American Institute of Physics, 2010, pp. 491-496.

[146] I. Mann, E. Murad, A. Czechowski, Planet. Space Sci. 55 (2007) 1000

[147] I. Mann, H. Okamoto, T. Mukai, H. Kimura, Y. Kitada, Astron. Astrophys. 291 (1994) 1011-1018.

[148] I. Mann, M. Köhler, H. Kimura, A. Czechowski, T. Minato, Astron. Astrophys. Rev. 13 (2006) 159-228.

[149] I. Mann, A. Czechowski, N. Meyer-Vernet, A. Zaslavsky, H. Lamy, Plasma Phys. Contr. Fus. 52 (2010) 124012.

[150] I. Mann, H. Kimura, D.A. Biesecker, et al., Space Sci. Rev. 110 (2004) 269.

[151] I. Mann, A . Pellinen-Wannberg, E. Murad, et al. Space Sci. Rev. 161 (2011) 1-47.

[152] E. Marsch, Living Rev. Solar Phys. 3 (2006) 1.

[153] T. Matsumoto, M. Kawada, H. Murakami, et al. Pub. Astron. Soc. Japan 48 (1996) L47-L51.

[154] T. L. Murdock, S. D. Price, Astron. J. 90 (1985) 375-386.

[155] N. McBride, J.A.M. McDonnell, Planet. Space Sci. 47 (1999) 1005

[156] R.L. McNutt et al., Acta Astronautica 69 (2011) 767-776.

[157] L. Megner, J. Gumbel, J. Atmos. Solar Terr. Phys. 71 (2009) 1236-1244.

[158] D. A. Mendis, Astrophys. Space Sci. 176 (1991) 163-167.

[159] D. A. Mendis, M. Rosenberg, Ann. Rev. Astron. Astrophys. 32 (1994) 419-463.

[160] N. Meyer-Vernet, Astron. Astrophys. 105 (1982) 98-106.

[161] N. Meyer-Vernet, Adv. Space Res. 209 (1985) 5.37-46.

[162] N. Meyer-Vernet, Am. J. Phys. 61 (1993) 249-257.

[163] N. Meyer-Vernet, Eur. J. Phys. 20 (1999) 167-176.

[164] N. Meyer-Vernet, In: Harris, R. A. (Ed.), 7th Spacecraft Charging Technology Conf., ESA SP-476, Nordwijk, ESTEC, (2001) 635.

[165] N. Meyer-Vernet, Basics of the Solar Wind, first ed. Cambridge University Press, Cambridge, UK, 2007.

[166] N. Meyer-Vernet, A. Zaslavsky, in: I. Mann, N. Meyer-Vernet, A. Czechowski (Eds.), Nanodust in the solar system: discoveries and interpretations, Springer, Heidelberg, 2012, pp.133-160.

[167] N. Meyer-Vernet, P. Couturier, S. Hoang, C. Perche, J.-L. Steinberg, Geophys. Res. Lett. 13 (1986) 279-282.

[168] N. Meyer-Vernet et al., Solar Phys. 256 (2009) 463–474.

[169] T. Minato, M. Koehler, H. Kimura, I. Mann, T. Yamamoto, Astron. Astrophys. 452 (2006) 701-707.

[170] E. Möbius, Space Sci. Rev. 143 (2009) 465-473.

[171] G.E. Morfill, E. Grün, Planet. Space Sci. 55 (1979) 1269-1282.

[172] G.E. Morfill, E. Grün, Planet. Space Sci. 55 (1979) 1283-1292.

[173] A. Morlok, C. Koike, N. Tomioka, I. Mann, K.Tomeoka, *Icarus* 207 (210) 45-58.

[174] T. G. Müller and 32 co-authors, Earth Moon Planet. 105 (2009) 209Ð219.

[175] T. Mukai, Astron. Astrophys. 99 (1981) 1-6.

[176] E. W. Muller, T. T. Tsong, Field Ion Microscopy, Elsevier, New York, 1969.

[177] G. M. Natanson, Sov. Phys. Tech. Phys., Engl. Transl. 5 (1960) 538-551.

[178] D. Nesvorny, D. Vokrouhlicky, W.F. Bottke, M. Sykes, Icarus 181 (2006) 107-144.

[179] D. Nesvorny, P. Jenniskens, H. F. Levison, W. F. Bottke, D. Vokrouhlicky, M. Gounelle, Astrophys. J. 713 (2010) 816-836.

[180] F. M. Neubauer, K.-H. Glassmeier, A. J. Coates, et al., Geophys. Res. Lett. 17 (1990) 1809-1812.

[181] T.G. Northrop, 1963, "Adiabatic motion of charged particles", Wiley, New York 1963.

[182] P. Oberc, W. Parzydlo, O. L. Vaisberg, Icarus 86 (1990) 314-326.

[183] P. Oberc, W. Parzydlo, Icarus 98 (1992) 195-206.

[184] P. Oberc, Adv. Space Res. 17, (12) (1996) 105.

[185] L.M. Ozernoy, in: M. Harwit (Ed.), The Extragalactic Infrared Background and its Cosmological Implications, Proceedings of IAU Symposium 204, ASP Conference Series, 2001, pp. 17-34.

[186] E. N. Parker, Astrophys. J. 128 (1958) 664-676.

[187] Parker, E.N., 2010, in: M. Maksimovic, K. Issautier, N. Meyer-Vernet, M. Moncuquet, F. Pantellini (Eds.), 12th International Solar Wind Conference, AIP CP1216, American Institute of Physics, 2010, pp. 8-13.

[188] V. Pierrard, M. Lazar, Solar Phys. 267 (2010) 153-174 .

[189] P.A.R. Ade, N. Aghanim, C. Armitage- Caplan and Planck collaboration, Astron. Astrophys. in print ArXiv e-prints arXiv:1303.5074.

[190] J. M. C. Plane, Chemical Society Reviews, 41(2012) 6507-6518.

[191] F. Postberg, S. Kempf, D. Rost, et al. Planet. Space Sci. 57 (2009) 1359-1374.

[192] J.H. Poynting, Philosophical Transactions of the Royal Society of London, Series A, 202 (1904) 346-358.

[193] S. M. L. Prokopenko, J. G. Laframboise, J. Geophys. Res. 85 (1980) 4125-4131.

[194] M. Rapp, F.-J. Lübken, J. Atmos. Solar Terr. Phys. 63 (2001) 759-770.

[195] M. Rapp, F.-J. Lübken, T. A. Blix, Adv. Space Res. 31 (2003) 2033-2043.

[196] M. Rapp, F.-J. Lübken, Atmos. Chem. Phys. 4 (2004) 2601-2633.

[197] Reach, W. T. Reach, B. A. Franz, T. Kelsall, J. L. Weilland, American Institute of Physics Conference Series 348 (1996) 37-46.

[198] W.T. Reach, P. Morris, F. Boulanger, K. Okumura, K., Icarus 164 (2003) 384.

[199] W. T. Reach, M. S. Kelley, M. V. Sykes, Icarus 191 (2007) 298-322.

[200] S. Redfield, Space Sci. Rev. 143 (2009) 323-331.

[201] S. Redfield, J. L. Linsky, Astrophys. J. 534 (200) 825-837.

[202] S. Redfield, J. L. Linsky, Astrophys. J. Sup. Ser. 139 (2002) 439-465.

[203] S. Redfield, J. L. Linsky, Astrophys. J. 673 (2008) 283-314.

[204] J. D. Richardson, J. C. Kasper, C. Wang, J. W. Belcher, A. J. Lazarus, Nature 454 (2008) 63-66.

[205] F.J.M. Rietmeijer, Meteoritics Planetary Science 35 (2000) 1025-1041.

[206] F. Rietmeijer, Chemie der Erde - Geochemistry 62 (2002) 1-45.

[207] M. T. Rietveld, B. Isham, EOS Transactions 82 (2001) 273-281.

[208] P. Riley, in: M. Maksimovic, K. Issautier, N. Meyer-Vernet, M. Moncuquet, F. Pantellini (Eds.), 12th International Solar Wind Conference, AIP CP1216, American Institute of Physics, 2010, pp. 323-328.

[209] H.P. Robertson, Mon. Not. Roy. Astron. Soc. 97 (1937) 423.

[210] M. Rosenberg, D. A. Mendis, J. Geophys. Res. 97, E9 (1992) 14,773-14,776.

[211] M. Rowan-Robinson, B. May, Mon. Not. Roy. Astron. Soc. 429 (2013) 2894-2902.

[212] M. Rowan-Robinson, J. Hughes, K. Vedi, D. W. Walker, Mon. Not. Roy. Astron. Soc. 246 (1990) 273.

[213] M. Rowan-Robinson, M. Jones, K. Leech, K. Vedi, J. Hughes, Mon. Not. Roy. Astron. Soc. 249 (1991) 729-741.

[214] K. Scherer, J. Geophys. Res. 105 (2000) 10329-10341.

[215] M. Smirnova, Dissertation (2011) Swedish Institute of Space Physics, Kiruna Sweden.

[216] M. Smirnova, E. Belova, S. Kirkwood, Ann. Geophys. 30 (2012) 457-465.

[217] L. Spitzer, Jr, Physical processes in the interstellar medium, Whiley, 1978

[218] E. J. Sternglass, Sci. Pap. 1772 (1954) Westinghouse Res. Lab., Pittsburg, Pa.

[219] M. Stix, The Sun, Springer Heidelberg, 2002, pp. 305-382.

[220] G.E. Thomas, J.J. Olivero, E.J. Jensen, et al. Nature 338 (1989) 490-492.

[221] N. Tomioka, K. Tomeoka, K. Nakamura-Messenger, T. Sekine, Meteoritics and Planetary Science, 42 (2007) 19.

[222] A. Tuzzolino et al., Science 304 (2004) 1776-1780.

[223] B.T. Tsuruntani, D.R. Clay, L.D. Zhang, et al., Icarus 167 (2004) 89-99.

[224] N.G. Utterback, J. Kissel, Astron. J. 100 (1990) 1315.

[225] N.G. Utterback, J. Kissel, Astrophys. Space Sci. 225 (1995) 327.

[226] E.F. van Dishoeck Annu. Rev. Astron. Astrophys. 42 (2004)119Ð167

[227] J.F. Vedder, J. ÐC. Mandeville, J. Geophys. Res. 79 (1974) 3247-3256.

[228] U.G. Wannberg and 35 co-authors, Radio Science Bulletin 332 (2010) 75-88.

[229] W. D. Watson, Astrophys. J. 176 (1972) 103-110.

[230] K. Weiss-Wrana, Astron. Astrophys. 126 (1983) 240-250.

[231] E. C. Whipple, Rep. Prog. Phys. 44 (1981) 1197-1250.

[232] E. C. Whipple, T. G. Northrop, D. A. Mendis, J. Geophys. Res. 90 (1985) 7405-7413.

[233] E. C. Whipple, in: N. Singh, K. H. Wright, Jr, N. H. Stone (Eds.), Current Collection from Space Plasmas, NASA CP 3089, 1990, pp. 1-12.

[234] A. N. Witt, S. Mandel, P. H. Sell, T. Dixon, U. P Vijh, Astrophys. J. 679 (2008) 497-511.

[235] M. Witte, H. Rosenbauer, M. Banaszkiewicz, Adv. Space Res. 13 (1993) 121-124.

[236] M. Witte, Astron. Astrophys. 426 (2004) 835-844.

[237] D. H. Wooden Space Sci. Rev. 138 (2008) 75-108.

[238] B. E. Wood, S. Redfield, J. L. Linsky, M. S. Sahu, Astrophys. J. 581 (2002) 1168-1179.

[239] M.C. Wyatt, in: Z. Knezevic, A. Milani (Eds.), Dynamics of populations of planetary systems, Cambridge University Press, Cambridge, (2005) pp. 383-392.

[240] S. Yamamoto, M. Mukai, Earth, Planets, and Space 50 (1998) 531-537.

[241] S. Yamamoto, M. Mukai, Astron. Astrophys. 329 (1998) 785-791.

[242] G.P. Zank, Space Sci. Rev. 89 (1999) 413-688.

[243] A. Zaslavsky, N. Meyer-Vernet, I. Mann, et al. J. Geophys. Res. 117, (2013) A05102, doi:10.1029/2011JA017480

[244] H. A. Zook et al., Science 274 (1996) 1501.

[245] H.A. Zook, in: B. Peucker-Ehrenbrink, B. Schmitz (Eds.) Accretion of extraterrestrial matter throughout EarthÕs history, Kluwer, New York, (2001) pp. 75-92.